5
Modeling and Technologies of Ultrafast Fiber Lasers

Brandon G. Bale, Oleg G. Okhitnikov, and Sergei K. Turitsyn

5.1
Overview of Short Pulse Fiber Lasers

5.1.1
Introduction

The generation and control of ultrashort optical pulses are rapidly growing areas of photonics with many emerging applications. This is primarily due to the fact that short optical pulses allow the probing of basic physics of light/matter interactions in the sub-picosecond regime, which in turn has opened up a range of new applications from high-bit-rate optical telecommunications to material processing at fundamental frequencies, usually around 1 μm, in addition to various biomedical diagnostics at frequency-doubled wavelengths. The requirements for simplicity, maintenance, and reliability, however, have not been met by conventional ultrafast technology, formerly based on solid-state lasers. Over the past decade much attention has been given to fiber lasers for the generation of ultrashort pulses, owing to various advantages it has over other solid-state lasers. Indeed, the recent growth of the telecom industry has resulted in the development of a mature fiber technology with reliable and cost-effective components, which makes suitably designed fiber lasers real contenders as alternatives to conventional solid state lasers. The waveguide geometry of fiber lasers not only simplifies many alignment issues, it also distributes heat generated by optical pumping over the length of the fiber. This is significant for reducing both the thermal management of the laser as well as the risk of damage to the medium itself. To achieve higher energies, fiber lasers have the potential for power scalability by implementing cladding pumping technology, which renders them ideal light sources for boosting the energy and brightness, with relative immunity from the thermal problems that have a serious impact on solid-state lasers via thermal lensing. Another attractive feature of optical fiber is the broad emission linewidth of a glass host, in contrast to crystalline hosts conventionally employed by bulk solid-state-lasers. The broad fluorescence spectrum makes different fiber gain media attractive for wavelength tunable continuous wave (CW) or pulsed sources. Most ultrafast laser systems

Fiber Lasers, First Edition. Edited by Oleg G. Okhotnikov.

are based on mode-locked oscillators. Active mode-locking relies on a loss or phase modulator, such as an acousto-optic modulator, inside the resonator. Passive mode-locking techniques are those that utilize the light in the cavity to cause a change in some intracavity element, which will then itself produce a change in the intracavity light. Typically, this is done with some form of a saturable absorber that has low loss for high intensities and high loss for low intensities. Passive techniques are simpler and allow for a much faster perturbation of cavity characteristics, which in turn results in shorter pulses. In addition to the intensity discrimination element, in an ultrashort passively mode-locked fiber laser there are various other physical effects, including group velocity dispersion (GVD), nonlinearity through self-phase modulation (SPM), saturable gain, bandwidth limited gain, and output coupling, among others. In this chapter we focus on modeling and technologies of ultrafast fiber lasers. In addition to describing the modeling equations used to numerically simulate the laser, we also derive a reduced model that is capable of capturing the overall laser dynamics at a significantly reduced computational cost. The reduced model is used to optimize system performance for desired output pulse characteristics, and highlights the key parameters in the laser. We then show how these parameters can be experimentally controlled using modern technologies and discuss their implementation in mode-locked fiber lasers. The chapter is organized as follows. In the following subsections we briefly discuss the main properties key components of passively mode-locked fiber lasers. In Section 5.2 we discuss the relevant modeling equations, discuss possible operating regimes, and derive a reduced model that can be used for optimization purposes. In Section 5.3 we discuss some recent experimental results of mode-locked fiber lasers, with particular emphasis on saturable absorber and dispersion control. Finally, in Section 5.4 we conclude and give some future perspectives.

5.1.2 Gain Fiber

Rare-earth doped silica fibers can provide the required gain for amplification in a fiber amplifier or laser [1]. Owing to the energy level structure of the dopants, the gain fiber determines many critical properties such as the wavelength range of operation, threshold, pump conversion efficiency, and wavelength tunability. Historically, erbium-doped fiber amplifiers were extensively developed and used for long-range optical communications networks since they amplify light around the 1.55 μm wavelength region, where standard telecom fibers have minimum loss [2, 3]. Thus, unsurprisingly, many early studies on fiber lasers relied on such a gain fiber and produced CW or pulsed light around the 1.55 μm wavelength. In addition to the traditional gain medium based on erbium-doped fiber, fibers using other rare-earth ions such as neodymium and ytterbium as dopants allow us to significantly extend the achievable spectral range towards the visible, from 970 to 1150 nm, and to achieve higher power levels. In this broad wavelength range there are several applications ranging from micro-machining at fundamental wavelengths to biomedical applications at frequency-doubled wavelengths. Ytterbium-doped silica fibers are of

particular significance since they have a broad gain bandwidth, high optical conversion efficiency, and large saturation fluence, offering an almost ideal gain medium for the generation and amplification of potentially high power, wavelength-tunable CW or pulsed radiation [4, 5]. Ultrashort pulse generation in a Yb-doped fiber laser was demonstrated [6, 7], and shortly after that configurations for higher energy pulses [8] and wavelength tunability were achieved [9]. Certain operation wavelengths in ytterbium-doped mode-locked fiber lasers are desirable, such as 980 nm, where a high emission cross section at this wavelength allows for very high gain in a short length of optical fiber, thus avoiding unwanted nonlinear effects. Further, the ability to frequency double the signal allows wavelengths to be obtained well into the visible region widely used in several applications, thus replacing bulky and inefficient Ar-ion lasers. In addition to fiber lasers operating towards the visible from the traditional 1.55 μm wavelength, it is also possible to use rare-earth dopants to extend the operation wavelength towards the infrared. For example, thulium- and thulium–holmium-doped fibers have been used for high-power sources operating around 2 μm [1]. Thulium fiber has a broad amplification bandwidth between 1.65 and 2.1 μm and is, therefore, suitable for short pulse generation and wide spectral tuning. Indeed, Thulium-doped fibers exhibit a particularly wide fluorescence spectrum and a tuning range up to 100 nm was demonstrated. Thulium also exhibits a significant advantage over other rare-earth ions in that the slope efficiency can exceed the Stokes limit, which is of interest for high-power laser systems. Thulium fiber lasers have been demonstrated [10] and ultrafast pulse generation has been achieved since the mid-1990s [11, 12] and is still an active area of research.

Although using different rare-earth ions in the gain medium can result in many desired properties such as power and operation wavelength, it is critical to understand how the dopant properties influence the operation characteristics of the other components of the cavity. For example, the operation wavelength will determine the value of the GVD coefficient in any passive fiber components in the cavity, and this must be compensated in some way, highlighting the role of dispersion control. Additionally, using a dopant that allows for higher power pulses could potentially induce significant SPM phase modulations, leading to unwanted instabilities. In Section 5.3 we will discuss various experimental mode-locked fiber laser set-ups utilizing both ytterbium- and thulium–holmium-doped fibers.

5.1.3
All-Fiber Methods for Dispersion Control

Dispersion management is a crucial aspect in ultrafast technology that allows for short, high-energy pulse generation through intracavity compensation and/or external pulse chirping/compression. Various methods have been applied for dispersion manipulation, including bulk components such as prism sequences, grating pairs, Gires–Tournois interferometer (GTI), and chirped mirrors [13]. These methods have been used extensively in solid-state lasers to tune the total dispersion of the cavity to either the normal or anomalous regime. In fiber-based systems the amount of dispersion induced by the optical fiber is typically large. The most common method

for providing negative dispersion in the laser cavity is to use a prism sequence. However, in ytterbium- and neodymium-doped fiber lasers the high value of normal material dispersion results in a large prism separation of approximately 1 m for adequate compensation. Using such bulk elements negates some of the potential advantages of fiber lasers. Specifically, it introduces potential alignment penalties, reduces the compactness of the device, and increases the cost.

Dispersion compensation would preferably be achieved by using components that preserve the all-fiber design of the cavity. Recently, specialty telecom dispersion shifted fibers were used at 1.55 μm wavelength in an ultra-long Er-doped mode-locked fiber laser to provide positive dispersion, leading to high energy pulses [14]. Other routes have focused on gratings and microstructured fibers. A fiber Bragg grating (FBG) is a type of distributed Bragg reflector constructed in a short segment of optical fiber that reflects particular wavelengths of light and transmits all others [15, 16]. This is achieved by adding a periodic variation to the refractive index of the fiber core, which generates a wavelength specific dielectric mirror. A fiber Bragg grating can therefore be used as an inline optical filter to block certain wavelengths, or as a wavelength-specific reflector. The refractive index profile of the grating may be modified to add other features, such as a linear variation in the grating period, called a chirp. The reflected wavelength changes with the grating period, broadening the reflected spectrum. A grating possessing a chirp has the property of adding dispersion, namely, different wavelengths reflected from the grating will be subject to different delays [17]. These so-called chirped fiber Bragg gratings (CFBGs) allow for large dispersion compensation in a short length of fiber. Another alternative for fiber dispersion compensation is to use a microstructured fiber that obtains its waveguide properties not from a spatially varying glass composition but from an arrangement of very tiny and closely spaced air holes that go through the whole length of the fiber (see, for instance, References [18, 19]). Solid-core index-guided photonic crystal fiber typically has a triangular pattern of air holes, with one hole missing. The guiding properties of this type of PCF (photonic crystal fiber) can be roughly understood with an effective index model: the region with the missing hole has a higher effective refractive index, similar to the core in a conventional fiber. There are also so-called photonic bandgap (PBG) fibers where light is confined in a hollow core due to a photonic bandgap that arises from a regular two-dimensional array of air holes in the cladding. It is possible for these fibers to provide anomalous dispersion at wavelengths well below the zero-dispersion wavelength of fused silica. Indeed, there is substantial design freedom with these microstructured fibers, allowing for different combinations of dispersion parameters. Although all-fiber dispersion compensation is useful since it maintains an all-fiber format for the laser, there are some potential pitfalls to consider when using the aforementioned techniques. Both dispersion shifted fibers and PBG fibers can suffer from large higher order dispersion. PBG fibers and CFBGs usually impose some form of bandwidth limitation, and in the case of CFBGs achieving the necessary bandwidths can require a large chirp value, which degrades the reflectivity properties of the grating. In Section 5.3 we will discuss various experimental set-ups using such fiber dispersion compensation elements.

5.1.4
Advanced Saturable Absorbers

In addition to fiber propagation, a saturable absorber is used to obtain a self-amplitude modulation of the light inside the laser cavity. Such an absorber introduces some loss to the intracavity laser radiation, which is relatively large for low intensities but significantly smaller for a short pulse with high intensity. Thus, a short pulse then produces a loss modulation because the high intensity at the peak of the pulse saturates the absorber more strongly than its low intensity wings. The loss modulation typically has an initially fast loss saturation determined by the pulse duration and potentially a somewhat slower recovery time that depends on the detailed mechanism of the absorption process. This saturable absorber mechanism allows self-starting mode-locking from normal noise fluctuations in the cavity. Various saturable absorber mechanisms can be used to achieve the desired intensity discrimination. So-called "artificial" saturable absorbers that rely on the optical Kerr effect have parameters that depend on the optical pulse itself, which is a consequence of its artificial behavior. These include, among others, the Kerr lensing [20], nonlinear polarization rotation [21], and nonlinear interferometry [22]. Indeed, these have all been implemented in applications in optical transmission, pulse regeneration, and the generation of ultrashort pulses. Non-artificial saturable absorbers have advantages over such methods since certain absorber parameters can be controlled in the manufacturing process. In this subsection we discuss two types of non-artificial saturable absorber mechanisms based on both semiconductor and carbon-based technologies.

5.1.4.1 Quantum-Confined Semiconductor Absorbers

Semiconductor saturable absorbers were used as early as 1974 in CO_2 lasers and were also utilized in the 1980s for diode lasers. For practicality a semiconductor saturable absorber is usually integrated with a semiconductor, dielectric, or metallic mirror, forming a semiconductor saturable absorber mirror (SESAM) [23]. Figure 5.1 shows schematically a conceptual picture of a SESAM structure. The quarter-wave AlAs/GaAs layers form the distributed Bragg reflector (DBR). Absorption is provided by a semiconductor material whose energy band-gap is set to match the wavelength of the optical signal to be controlled and it is usually embedded within semiconductor material(s) with a higher band-gap(s) that does not absorb the optical signal. The whole absorber region may consist of several quantum-well layers, representing the so-called multiple-quantum-well (MQW) structure. In Figure 5.1, for example, the absorption region consists of quantum wells, which for $\lambda \leq 1.1\,\mu m$ are made of GaInAs(P)/GaAs layers deposited onto a GaAs/AlAs DBR. For $\lambda \geq 1.3\,\mu m$ the quantum wells can be made of GaInAsP. Another approach is to alloy nitrogen with GaInAs to reduce the band-gap of the quaternary (due to a conduction band-bending effect) and prepare GaInNAs/GaAs quantum wells on a GaAs/AlAs DBR. Such a heterostructure has a wide operating range, from $0.94 \leq \lambda \leq 1.55\,\mu m$ (and even wider), representing a considerable spectral extension of the GaAs technology. Absorbing layers are usually placed at field maximum (antinodes of a standing wave)

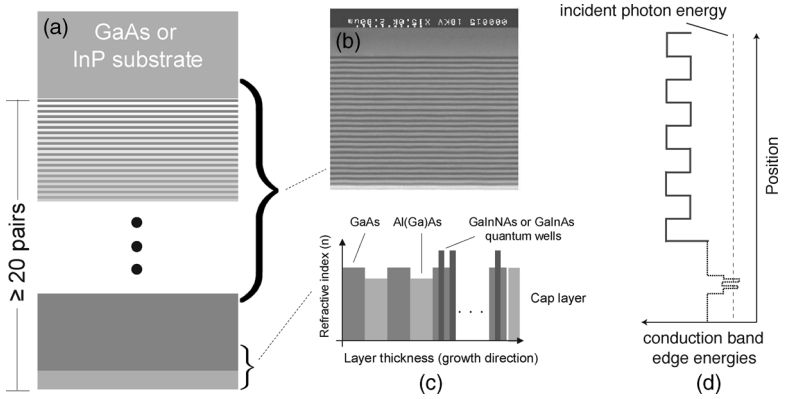

Figure 5.1 (a) Design of a monolithic SESAM for 1.3 μm operation. The quantum wells are made of GaInNAs/GaAs. The DBR consists of a stack of $\lambda/4n$ mirror pairs. The structure shown here is grown on a GaAs substrate by molecular beam epitaxy or metal–organic chemical vapor deposition (MOVPD); (b) SEM (scannable electron microscope) cross-section of the DBR section; (c) refractive index of the quantum well structure; (d) energy band diagram in a typical SESAM structure.

for enhanced interaction. The production of SESAM technology is well established and can be carried out either with molecular beam epitaxy (MBE) or with metal–organic chemical vapor deposition (MOVPD) [13]. The absorbing section can be enclosed in a Fabry–Perot cavity forming the resonant absorber. When used in a laser cavity, a SESAM introduces intensity-dependent losses and because the laser tends to operate with minimum cavity loss per round-trip the longitudinal modes of the lasers become phase-locked to reach low-loss state corresponding in the time domain to short optical pulses. Although SESAMs have primarily been used in solid-state lasers [13, 24–26], they have also been employed for mode-locking for various fiber lasers [27–29]. Using a SESAM in a fiber cavity eliminates the need for critical cavity alignment and it can be designed to operate in a wide spectral range [9].

Recently, there has been increasing interest in quantum dot (QD) based SESAMs due to their tunable optical properties. Based on technology used for the fabrication of quantum-well-based SESAMs, QD-based counterparts were first used for mode-locking in 2001 [30] and showed fast recovery dynamics as well as low saturation fluence at moderate modulation depth, which is difficult to obtain from QW-based SESAM structures. Shortly afterwards these properties were utilized for ultrashort pulse generation in mode-locked lasers [31–33]. QD-SESAMs have been particularly successful for mode-locking vertical external cavity surface emitting lasers, which allows for a high repetition rate and large average powers [34].

5.1.4.2 **Carbon-Based Absorbers**

Rapid advances in chemical synthesis and fabrication techniques generate novel types of nanometer-sized materials that exhibit original and often unforeseen

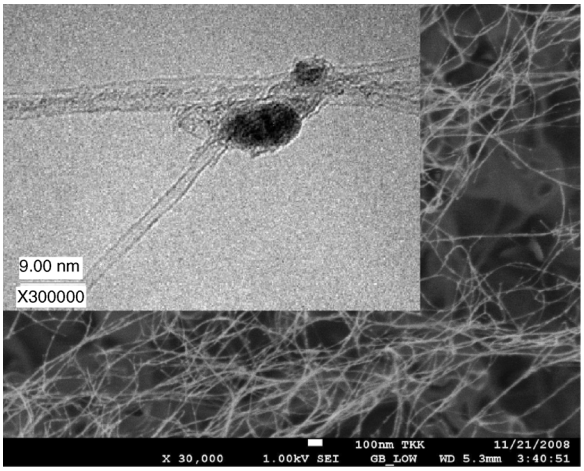

Figure 5.2 SEM micrograph of a SWCNT film. Inset: high-resolution transmission electron microscope (TEM) image of the sample. The tube diameter ranges from 1.2 to 1.8 nm.

properties, which can be controlled by the type of material, sample size, shape, and topology. One such material is single-walled carbon nanotubes (SWCNTs), which, because of their fast absorption (determined by the tube diameter), have saturable absorption or optically induced transparency in the near-infrared wavelength region around 1.0–2.0 μm [35]. Such saturable absorber SWCNTs have been fabricated through different processes that all primarily address the three steps of nanotube growth, dispersion, and deposition processes, typically with the CNTs (carbon nanotubes) being embedded in a polymer or liquid [36]. Figure 5.2 shows a SEM micrograph of a SWCNT film with tube diameter ranging from 1.2 to 1.8 nm [37]. The CNTs, together with the polymer-based material, have then been applied on the surface of an optical fiber or a quartz substrate for optical applications. Recently, various optical properties such as the absorption band and how it is controlled by tube diameter, chirality, and diameter distribution have been studied [38]. Indeed, it was shown that broadband absorption can be achieved for SWCNT samples with a large diameter distribution. However, this increases the overall loss since non-operation wavelengths will undergo significant losses. Different methods have been used to control the tube diameter and vary the diameter distribution of SWCNT products [36].

Passive mode-locking employing a saturable absorber SWCNT was demonstrated for both solid-state and fiber lasers [36, 39]. SWCNTs have been used in fiber laser systems with various dopants, as well as both linear and ring cavities since they can be fabricated to operate both in transmission or reflection. In a ring configuration, the SWCNT is directly deposited onto the fiber end-face, where for a linear cavity it would be deposited on a mirror that is at one end of the resonator. Polymer is undesirable as an intracavity laser material due to its relatively low damage threshold and high optical absorption. It should be avoided, especially for high power and mid-IR applications. New advances include ring configurations where the CNT interacts

with the evanescent field propagating in a thin fiber taper [40] as well as linear configurations with polymer-free SWCNT samples using a dry-transfer contact press method on a highly reflective mirror [37]. In this last approach broadband mode-locking was demonstrated using the same absorber deposited on an Ag-mirror for mode-locking of Yb-, Er-, and Tm:Ho-doped fiber lasers at 1.05, 1.56, and 1.99 μm, respectively, with sub-picosecond pulse durations [37]. In contrast, the reflection bandwidth of a SESAM is limited to about 100 nm due to the low index contrast in the GaAs/AlAs Bragg mirror and probably even more by the quantum well absorption characteristics. Indeed, SWCNTs can have many advantages over current state-of-the-art saturable absorbers due to their polarization insensitivity, high optical damage threshold, mechanical and environmental robustness, and ease of integration into optical systems.

Recently, graphene has been investigated as a promising saturable absorber that would avoid the intrinsic large losses associated with the various tube sizes in SWCNT samples. For a sufficient nonlinear response, however, it has been shown that few-layer graphene flakes should be employed. The optical absorption, ultrafast carrier relaxation time, and controllable modulation depth of the graphene have been actively measured [41]. So far, several graphene mode-locked fiber lasers have been demonstrated near 1.0 and 1.5 μm [42–44]. Wide-range wavelength tunability has been realized in both mode-locked and Q-switched fiber lasers. This area of research continues to be very active and the stability and optical damage of graphene in the ultrafast laser environment still need to be rigorously examined.

5.2
Modeling of Ultrafast Fiber Lasers

Modeling ultrashort pulse fiber lasers is a rather challenging problem from a computational standpoint. Numerical analysis of the building of short optical pulses from noise through many-round trips in a laser cavity requires substantial computational time. An even more complex computational problem is the optimization of laser operation in multi-dimensional space of system parameters and cavity geometry. Thus there is a need for simplified modeling that retains the physical nature of the laser cavity. The master model, introduced in the laser science context by Haus [45, 46], is commonly used for the analysis of pulsed mode-locked femtosecond or picosecond fiber lasers (see, for instance, Reference [47] and references therein). The master equation is a version of the complex Ginzburg–Landau equation and extends the well-known nonlinear Schrödinger equation (NLSE) to include dissipative terms. It is a distributed model and includes the key physical processes in a mode-locked fiber laser, including GVD, nonlinear phase accumulation through SPM, gain, and (nonlinear) amplitude modulation from the saturable absorber in a distributed way [47]. Studies of the Ginzburg–Landau equation reveal various possible steady state solutions ranging from hyperbolic secant solutions to localized optical waves in the normal dispersion regime with the characteristic sharp edged spectrum [48–51].

Although significant mathematical insight can be obtained from such an averaged model, this model fails when changes in the optical field amplitude and/or phase during a single round trip become substantial [52]. In modern mode-locked fiber lasers pursuing ultrafast, high-energy pulse generation, there are typically significant nonlinear dynamics during one cavity necessitating significant pulse changes per cavity round trip for stabilization. For example, the propagation of a high intensity pulse in an optical fiber can lead to significant spectral broadening along with changes of the optical field parameters during one round trip, breaking the assumption on which averaged mode-locked laser models are based. In this case a modified NLSE can only be used for modeling the optical field propagation through passive and active fibers. However, other discrete elements such as the saturable absorber, output coupling elements, filters, and so on should be considered separately from fiber propagation, and *not* be included in the modeling in a distributed way. In stable operation, the generated pulse should reproduce itself (up to the phase factor) after propagation over all laser system elements after one round trip. Mathematically this corresponds to so-called Poincaré mapping, which arguably is more appropriate to describe periodic laser dynamics than an averaged model. Including the discrete elements in the laser highlights the periodic nature of the resonator and strengthens the significance of the intracavity pulse dynamics. These dynamics can be optimized by varying both the system parameters of the laser as well as the laser configuration itself.

5.2.1
Numerical Modeling of Ultrashort Fiber Lasers

Pulse propagation in a rare-earth doped fiber can be modeled with a generalized nonlinear Schrödinger equation [53]:

$$\mathrm{i}U_z - \tfrac{1}{2}\beta_2 U_{tt} + \gamma|U|^2 U = \mathrm{i}\left[(g-\Gamma)U + \frac{g}{\Omega_g^2}U_{tt}\right] \tag{5.1}$$

where

$U(z,t)$ is the electromagnetic field envelope,
z is the propagation distance along the fiber,
t is the retarded time frame,
β_2 ($\mathrm{ps^2\,m^{-1}}$) is the group velocity dispersion coefficient,
γ ($\mathrm{W^{-1}\,m^{-1}}$) is the nonlinear coefficient,
Γ ($\mathrm{dB\,m^{-1}}$) is the linear loss coefficient,
and Ω_g (THz) is related to the width of a parabolic (in the frequency domain) filtering action.

This equation neglects higher order linear effects such third-order dispersion as well as higher order nonlinear effects such as self-steepening or intrapulse Raman scattering [53]. Although these effects can have noticeable effects for pulses shorter than 1 ps, here we neglect them as the leading order behavior is well approximated by

Table 5.1 Measured recovery time τ_g, intensity saturation $I_{s,g}$, and power saturation $P_{s,g} = I_{s,g} \times A_{eff}$ for typical dopants. This is not a complete list of the range of all parameter values – only examples are given of key parameters that can be used in the model equation (5.2) (see text for references).

Parameter	Erbium	Ytterbium	Thulium	Holmium
Recovery time τ_g (μs)	8–15	1–2	4–6	8–12
Intensity saturation $I_{s,g}$ (W cm^{-2})	0.2–1	25–100	0.5–5	0.5–1.5
Power saturation $P_{s,g}$ (mW)	0.1–5	10–20	0.5–10	10–100

(5.1). The gain dynamics can be modeled by a 2-level approximation leading to a rate equation for the gain parameter g (dB m^{-1}) [2, 54]:

$$\frac{\partial g(z,t)}{\partial t} = \frac{g_0 - g(z,t)}{\tau_g} - \frac{g(z,t)|U(z,t)|^2}{P_{s,g} \times \tau_g} \tag{5.2}$$

where

g_0 (dB m^{-1}) is the small signal gain,
Q3 τ_g (ms) is the inversion relaxation time,
$P_{s,g}$ (mW) is the power saturation of the gain medium.

Table 5.1 shows some of the measured values of key macroscopic parameters for commonly used rare-earth dopants. We see that there is a significant range of parameter values, depending on particular advanced fabrication processes. Here we note that the power saturation is simply the intensity saturation multiplied by the effective cross area of the fiber. This table does not include all possible parameter regimes, but highlights only some of the values that have been reported in References (erbium) [2, 3, 55, 56], (ytterbium) [4, 5, 57–59], (thulium) [60–64], and (holmium) [65–67]. For ultrafast pulse generation the gain relaxation time is much longer than the pulse durations T_0 ($T_0 \ll \tau_g$). Thus we would not expect the optical field to change the gain g significantly over one cavity round trip. However, the optical field over a longer time scale (over many round trips) will have an effect on the gain. Here we assume that on this longer time scale the gain will have a stationary value ($\partial g/\partial t = 0$). The gain will have saturated over many pulses, or in other words with the average power $\langle |U|^2 \rangle = E_p/T_R$, where E_p is the pulse energy and T_R is the round trip time of the laser. Setting the right-hand side of Equation 5.2 to zero and letting $|U(z,t)|^2 \to \langle |U|^2 \rangle$, we obtain:

$$g(z,t) = g(z) = \begin{cases} g_0/[1 + E(z)/(P_{s,g}T_R)] & \text{for active fiber,} \\ 0 & \text{for passive fiber} \end{cases} \tag{5.3}$$

where the pulse energy $E(z) = \int_{-\infty}^{\infty} |U(z,t)|^2 \, dt$. Note that in this limit the relaxation time is not a parameter in (5.3), but the relevant time scale is the round trip time T_R, which determines the effective saturation energy $P_{s,g} \times T_R$.

In addition to fiber propagation, the pulse experiences action induced by the discrete elements in mode-locked fiber lasers. As has been discussed in previous section, various saturable absorber mechanisms have been implemented in mode-locked lasers. The microscopic properties of such devices can be modeled to reveal the macroscopic quantities that are important for saturable absorption. In our approach we neglect the detailed microscopic properties of a particular saturable absorber and assume a general rate equation [45]:

$$\frac{\mathrm{d}q(t)}{\mathrm{d}t} = -\frac{q(t)-q_0}{\tau_\mathrm{A}} - \frac{q(t)|U_\mathrm{i}(t)|^2}{P_{\mathrm{s},A} \times \tau_\mathrm{A}} \tag{5.4}$$

where

$q(t)$ is the saturable absorber loss coefficient that does not include any non-saturable losses,
$|U_\mathrm{i}(t)|^2$ is the time-dependent power incident on the absorber,
$1-q_0$ is the modulation depth,
$P_{\mathrm{s,A}}$ is the saturation power,
τ_A is the absorber recovery time.

By solving Equation 5.4 we can determine the saturable absorption $q(t)$ as a function of time and the input field. The output pulse power can then be found from the relation $|U_\mathrm{f}(t)|^2 = [1-q(t)]|U_\mathrm{i}(t)|^2$, where $U_\mathrm{i}(t)$ ($U_\mathrm{f}(t)$) is the input (output) field. Notably, the saturable absorber rate equation (5.4) is very similar to the gain rate equation (5.2). As in the case for the gain rate equation, the rate equation has particular limits depending on the saturation recovery time. In the case when the absorber recovery time is much faster than the pulse duration ($\tau_\mathrm{A} \ll T_0$), we can assume that the absorption instantaneously follows the absorption of the incident power $|U_i(t)|^2$ and Equation 5.4 reduces to:

$$0 = -[q(t)-q_0] - \frac{q(t)|U_\mathrm{i}(t)|^2}{P_{\mathrm{s,A}}} \tag{5.5}$$

giving a transfer function:

$$U_\mathrm{f}(t) = \left[1 - \frac{q_0}{1+|U_\mathrm{i}(t)|^2/P_{\mathrm{s,A}}}\right] \times U_\mathrm{i}(t) \tag{5.6}$$

Table 5.2 shows measured values of key macroscopic parameters for some of the non-artificial saturable absorbers discussed previously. We see that there is a significant range of parameter values, depending on particular advanced fabrication processes. The table does not include all possible parameter regimes, but only highlights those obtained from more recent fabrication discussed in References (SESAM-QW) [68–70], (SESAM-QD) [71, 72], (CNT) [36, 37, 73, 74], and (graphene) [75–77].

Often it is necessary to output some of the signal in the optical system. The discrete action of the output coupler can be approximated by a simple scalar multiplication of the field:

Table 5.2 Measured recovery time τ_A, saturation fluence $S = P_{s,A}\tau_A/A_{eff}$, modulation depth $1-q_0$, and insertion loss for various fabrication processes. This is not a complete list of the range of all parameter values – only examples are given of key parameters that can be used in the model Equation 5.4 (see text for references).

Parameter	SESAM-QW	SESAM-QD	CNT	Graphene
τ_A (ps)	0.1–100	0.7–100	<1	0.1
S (μJ cm^{-2})	1–1000	14–60	3–35	2–300
$1-q_0$ (%)	0.1–70	0.2–17	1–20	4–70
Insertion loss (%)	<0.1	<0.2	4–80	35–70

$$U_f(t) = \sqrt{R} \times U_i(t) \tag{5.7}$$

In this approximation we are assuming that the output coupler is only an amplitude modulation and any phase modulations are assumed to be small, so that the laser output field would be given by $\sqrt{1-R} \times U_i(z,t)$. Finally, we consider the discrete action of a spectral filter $\hat{A}(\omega)$ on the pulse. The pulse form is modified in both amplitude and phase and can be written as:

$$U_f(t) = \int_{-\infty}^{\infty} \hat{U}_i(\omega) \times \hat{A}(\omega) e^{-i\omega t}\, d\omega \tag{5.8}$$

where $\hat{U}_i(\omega)$ denotes the Fourier transform of $U_i(t)$.

Including all effects of pulse propagation in passive and active fibers as well as the discrete elements of the saturable absorber, output coupler, and spectral filter allows for stable and robust mode-locking in various experimentally realized configurations. Various operation modes exist and it is customary to define these modes by classifying the resultant intracavity pulse evolutions.

5.2.2
Classification of Pulsed Fiber Lasers

In general, the intracavity dynamics of the optical pulse in a fiber laser cavity can range from stationary solutions to heavily breathing solutions, depending on the dispersion elements in the cavity. A pulse propagating in an optical fiber acquires a nontrivial temporal phase shift. The concavity of the nontrivial phase, or the sign of the chirp, multiplied by the dispersion value of the fiber determines whether the pulse is undergoing compression or broadening [53]. In general, an ultrashort pulse propagating in a mode-locked fiber laser can have the following intracavity dynamics:

- Static soliton propagation
- stretched pulse propagation,
- propagation in the normal dispersion regime,

–high intensity parabolic pulse propagation in passive fibers,
–static gain-guided solitons,

–similariton propagation in active fibers,
–dissipative soliton propagation.

In the following we describe such propagation regimes in mode-locked fiber lasers.

Optical solitons are stationary solutions (no breathing dynamics) that rely on a delicate balance between the fiber nonlinearity and dispersion. The soliton does not have a nontrivial phase across it since the positive phase modulation from fiber nonlinearity nearly cancels the negative phase modulation induced by the fiber dispersion. Because the concavity of the nontrivial phase is zero, the pulse dynamics are stationary. In 1992 the first all-fiber ring cavity produced stable soliton pulses [78]. This, and many other mode-locked fiber lasers that followed, used an operating wavelength of 1.55 μm, where an erbium-doped fiber was used as an amplifying medium and standard telecom fibers have anomalous dispersion. Although these lasers were able to produce stable femtosecond pulses, the output pulse characteristics are restricted by fundamental properties of the soliton. Similar to guiding center solitons in optical communications [79, 80], a soliton becomes highly unstable due to side-band instabilities when the period of perturbations approaches $8Z_0$, where $Z_0 = T_0^2/(2|\beta_2|)$ is the soliton period and T_0 is the pulse duration [81]. Because a mode-locked laser periodically perturbs the pulse at the cavity round-trip length L, the shortest soliton that can be supported stably must have $T_0^2 = |\beta_2|L/4$. For a fiber laser composed of standard optical fiber operating at 1.55 μm (where $\beta_2 \sim -0.02$ $\mathrm{ps}^2\,\mathrm{m}^{-1}$) of length $L = 1$ m, this restricts the pulse duration to ~ 70 fs. If we require 10 fs pulses from the cavity the length of the fiber should be reduced to $L = 2$ cm, which is not very practical. This instability thus imposes a lower limit on the achievable pulse duration with a soliton laser. In addition to this lower bound for the pulse duration, the pulse energy is bounded above due of the delicate balance between dispersion and nonlinearity, which gives the soliton area theorem $E_{\mathrm{sol}} = |\beta_2|/(2\gamma T_{\mathrm{sol}})$. Since the pulse duration is typically limited to ~ 100 fs due to the aforementioned side-band instabilities, the pulse energy from such lasers is bounded above by ~ 0.1 nJ.

To overcome these limitations on the pulse output when using fiber for the waveguide medium, one can introduce positive dispersion into the cavity to achieve some form of dispersion management. The earliest attempt minimized pulse shaping in optical fiber by using short lengths of positive Er^{3+}-doped fiber along with prisms for negative dispersion in a linear cavity [82]. This technique demonstrated pulse durations of 84 fs with 10 pJ of energy; however the laser was not self-starting. Shortly after this, Tamura *et al.* introduced the stretched-pulse technique, which involves an all-fiber ring cavity that consists of segments of alternately large positive and negative dispersion fiber [83]. The key property of the stretched pulse operation is that the sign of the chirp oscillates between positive and negative values, with zeros near the middle of each dispersion segments. Because the sign of the product of the chirp and dispersion is also oscillating about zero, the pulse stretches and compresses twice per cavity round trip and has a minimum pulse duration at the zero-chirp points. In contrast to static soliton propagation, the pulse width can change by an order of magnitude within the cavity, which serves to lower the average peak power when compared with that of an unchanging

transform-limited pulse of the same bandwidth. This effectively allows for higher energy pulses with larger bandwidths, similar to dispersion-managed systems in transmission [84]. Although higher energies and powers are possible, such lasers will still be susceptible to soliton-like instabilities such as spectral pulse splitting and pulse break-up when the pulse obtains a large nontrivial phase in the anomalous dispersion fiber segment. Since the magnitude of the nontrivial phase is related to the peak power through SPM, this restricts the peak power, and thus the energy, of the pulse.

The restrictions that anomalous GVD fiber has on pulse propagation inspired a new generation of mode-locked fiber lasers operating with only positive dispersion fiber segments. Elimination of the anomalous dispersion segment of a fiber laser is only possible if the pulse-shaping is not reliant on the cancellation of phase modulations from GVD and SPM. Parabolic self-similar pulse propagation in normal GVD fiber was used in a laser resonator in References [85–87]. The dispersion was compensated for by bulk elements such as a linear dispersive line or a grating pair. Pulse propagation largely relied on known propagation in optical fiber operating in the normal GVD regime with the pulse duration increasing and the chirp parameter going to zero for reasonable propagation lengths in passive fiber [88]. These lasers were successful in that they were able to generate femtosecond pulses with 10 nJ energies. The pursuit of higher energy pulses suggests laser cavities with larger positive dispersion, or even lasers that eliminate the anomalous GVD segments altogether. Pulse propagation in a normal dispersion fiber will have an increasing pulse duration and bandwidth as well as an increasing (in magnitude) negative chirp. A laser without anomalous GVD would presumably have to exploit dissipative processes to compensate this behavior. The so-called gain-guiding solitons are static solutions having a hyperbolic secant shape and rely on the balance of gain dispersion (or filtering) to compensate the broadened bandwidth caused by the normal GVD [89]. Chong *et al*. proposed the incorporation of a spectral filter in an all-normal dispersion laser and found "dissipative soliton" solutions with energies above 20 nJ and peak powers greater than 100 kW with standard fiber operating at 1 μm [90, 91]. Recently, a mode-locked fiber laser that supports amplifier similaritons has been theoretically proposed [92] and experimentally realized [93, 94]. Similariton solutions are pulses that evolve self-similarly in a fiber amplifier, holding certain relations between pulse characteristics. This laser relies on spectral filtering a similariton pulse generated in a doped fiber operating at normal dispersion. In lasers supporting parabolic solutions, dissipative solitons, or amplifier similaritons the pulse evolution is distinctly different from soliton or stretched pulse evolution. In such lasers, the pulse duration increases throughout the cavity while the chirp is always one sign. At a discrete point in the cavity the pulse duration, chirp, and bandwidth are compensated by a dissipative element [95].

Figure 5.3 highlights the pulse evolutions in the case of soliton, stretched pulse, and dissipative soliton and similariton pulse systems. In modeling Equations 5.1–5.8, self-starting mode-locking from initial white noise can be observed, and the resultant operating regimes and pulse evolutions depend on the multiple parameters involved as well as the geometry of the laser setup. In the next section we discuss a reduced

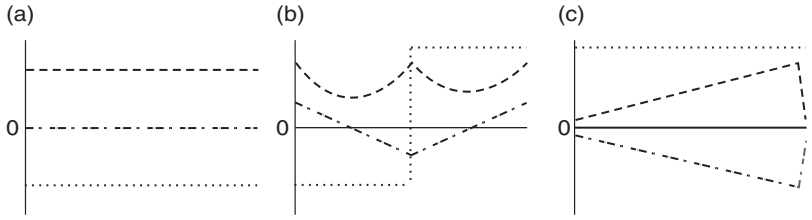

Figure 5.3 Different pulse evolutions per cavity round trip characterized by the behavior of the pulse duration (– – –) and chirp parameter (–·–·–). The dispersion map is denoted by the solid curve and is negative (positive) for anomalous (normal) dispersion. (a) Static soliton pulse evolution; (b) stretched pulse evolution; (c) all-normal dispersion evolution for dissipative solitons and amplifier similaritons in a resonator.

modeling approach that can be effective in the optimization of such complex multi-parametric systems.

5.2.3 Simplified Modeling Approach

Often, pulse dynamics in optical fiber can be captured by obtaining evolution equations of key pulse characteristics such as pulse width, peak power, energy, chirp parameter, and bandwidth [53]. The particle-like properties of pulses make it possible to derive under some reasonable assumptions a closed system of coupled ordinary differential equations (ODEs) that approximate well the key important features of the pulse dynamics. This important simplification is a direct consequence of the pulse being a wave-packet that can be well-approximated by a finite number of degrees of freedom. Instead of the analysis of the partial differential equation (5.1), one can use a finite set of ODEs to understand the pulse dynamics. Both the variational method and the method of moments have been used to derive such ODEs for nonlinear Schrödinger-type equations. The variational approach [96] relies on the ability to restate the NLSE in terms of a variational problem in which the Lagrangian is to be minimized for a particular *ansatz* function. It was first used for NLSE-type equations by Anderson in 1983 [97] and has since been extensively used to model various perturbed NLSE systems such as dispersion management in telecommunications [98, 99] as well as mode-locked lasers [100–102] (for a recent review see Reference [103] and references within). The method of moments (or root mean square momentum method), first used in nonlinear optics as early as 1971 [104], quantifies certain pulse characteristics such as pulse duration and peak power in terms of integral (over time) quantities. The governing partial differential equation can be algebraically manipulated, resulting in a set of ODEs describing the evolution (in z) of the integral quantities [105]. Here we focus on certain integral quantities called the root-mean-square (RMS) characteristics, which have been used successfully to describe, among others, pulse durations in fibers [106], pulse characteristics in lossy fibers [107], dispersion-managed systems [108–112], and mode-locked

lasers [113, 114]. To describe the key particle-like characteristics of the pulse field $U(z,t)$ we consider the evolution of the following integral quantities:

$$T_{\mathrm{RMS}}(z) = \left[\frac{\int t^2 |U(z,t)|^2 \,\mathrm{d}t}{\int |U(z,t)|^2 \,\mathrm{d}t}\right]^{\frac{1}{2}} \quad C_{\mathrm{RMS}}(z) = \frac{i}{4}\frac{\int t[U(z,t)\,U_t^*(z,t) - U^*(z,t)\,U_t(z,t)]\,\mathrm{d}t}{\int |U(z,t)|^2 \,\mathrm{d}t} \tag{5.9a}$$

$$P_{\mathrm{RMS}}(z) = \frac{\int |U(z,t)|^4 \,\mathrm{d}t}{\int |U(z,t)|^2 \,\mathrm{d}t} \quad \Omega_{\mathrm{RMS}}(z) = \left[\frac{\int |U_t(z,t)|^2 \,\mathrm{d}t}{\int |U(z,t)|^2 \,\mathrm{d}t}\right]^{\frac{1}{2}} \tag{5.9b}$$

which describe the RMS pulse duration T_{RMS}, pulse power P_{RMS}, chirp parameter C_{RMS}, and bandwidth Ω_{RMS}. All integrals are from $(-\infty, \infty)$. Through algebraic manipulation of Equation 5.1, and assuming that the nontrivial phase profile of the pulse is a quadratic function ($= C_{\mathrm{RMS}}/T_{\mathrm{RMS}}^2 \times t^2$) [115], we obtain:

$$\frac{\mathrm{d}P_{\mathrm{RMS}}}{\mathrm{d}z} = 2\beta_2 \frac{C_{\mathrm{RMS}} P_{\mathrm{RMS}}}{T_{\mathrm{RMS}}^2} + 2(g-\Gamma)P_{\mathrm{RMS}} + \frac{2g}{\Omega_{\mathrm{g}}^2}\left[I_3 + \Omega_{\mathrm{RMS}}^2 P_{\mathrm{RMS}}\right] \tag{5.10a}$$

$$\frac{\mathrm{d}T_{\mathrm{RMS}}}{\mathrm{d}z} = -2\beta_2 \frac{C_{\mathrm{RMS}}}{T_{\mathrm{RMS}}} - \frac{g}{(\Omega_{\mathrm{g}} T_{\mathrm{RMS}})^2}\left[-1 - T_{\mathrm{RMS}}^2 \Omega_{\mathrm{RMS}}^2 + I_1\right] \tag{5.10b}$$

$$\frac{\mathrm{d}C_{\mathrm{RMS}}}{\mathrm{d}z} = -\tfrac{1}{2}\beta_2 \Omega_{\mathrm{RMS}}^2 - \frac{\gamma}{4} P_{\mathrm{RMS}} + \frac{g}{\Omega_{\mathrm{g}}^2}\left[I_2 + 2C_{\mathrm{RMS}}\Omega_{\mathrm{RMS}}^2\right] \tag{5.10c}$$

$$\frac{\mathrm{d}\Omega_{\mathrm{RMS}}^2}{\mathrm{d}z} = -2\gamma \frac{C_{\mathrm{RMS}} P_{\mathrm{RMS}}}{T_{\mathrm{RMS}}^2} + \frac{2\mathrm{g}}{\Omega_{\mathrm{g}}^2}\left[\Omega_{\mathrm{RMS}}^4 - I_4\right] \tag{5.10d}$$

where:

$$I_1 = \int t^2 |u_t|^2 \,\mathrm{d}t/E,\ I_2 = i\int t\left(u_{tt}u_t^* - u_{tt}^* u_t\right)\mathrm{d}t/(2E),\ I_3 = \int |u|^2\left(uu_{tt}^* + u^* u_{tt}\right)\mathrm{d}t/E,$$
$$I_4 = \int |u_{tt}|^2 \,\mathrm{d}t/E, \text{ and } E = \int |u|^2 \,\mathrm{d}t$$

The dissipative terms introduce new momenta I_1 through to I_4 and thus a closed system of equations is not possible. However, we can reduce the system of equations (5.3) to describe the key pulse parameters by assuming a specific structural form of the pulse. Although this will introduce an additional approximation, since in addition to a quadratic phase profile across the pulse we are assuming a power profile as well, all RMS integrals can be explicitly computed, resulting in a closed system of ordinary equations. In general, any structural form can be used, for example, a chirped

hyperbolic secant, Gaussian, or parabolic pulse. To give a specific example, if we assume a chirped-Gaussian pulse of the form:

$$\sqrt{P(z)}\exp\left[-\frac{t^2}{2\tau(z)^2}(1-\mathrm{i}C(z))+\mathrm{i}\varphi(z)\right] \tag{5.11}$$

it is easy to compute from Equation 5.9 the RMS pulse characteristics $T_{\mathrm{RMS}}=\tau/\sqrt{2}$, $C_{\mathrm{RMS}}=C/4$, $P_{\mathrm{RMS}}=P/\sqrt{2}$, and $\Omega^2_{\mathrm{RMS}}=(1+C^2)/(2\tau^2)$ as well as the moments I_1 thru I_4. Substituting these values into Equation 5.10 gives:

$$P_z=\beta_2\frac{CP}{\tau^2}+2(g-l_0)P-\frac{2g}{\Omega_{\mathrm{g}}^2\tau^2} \tag{5.12a}$$

$$\tau_z=-\beta_2\frac{C}{\tau}-\frac{g}{\Omega_{\mathrm{g}}^2}\frac{1}{\tau}(C^2-1) \tag{5.12b}$$

$$C_z=\left[-\beta_2-\frac{2g}{\Omega_{\mathrm{g}}^2}C\right]\frac{1+C^2}{\tau^2}-\frac{\gamma}{\sqrt{2}}P \tag{5.12c}$$

In the limit in which the gain dynamics can be described by Equation 5.3, the gain in this reduced model is given by:

$$g=\begin{cases} g_0/[1+P\tau\sqrt{\pi}/(P_{\mathrm{s,g}}T_{\mathrm{R}})] & \text{for active fiber,}\\ 0 & \text{for passive fiber}\end{cases} \tag{5.13}$$

The reduced model for (5.12)–(5.13) can be used to model the pulse characteristics for fiber propagation. In this reduced model system it is also possible to include the discrete nature of the dissipative elements [100, 102]. This is possible under the approximation that each element is assumed not to change the pulse temporal and spectral profile. Using this approximation it is possible to describe large variations in the pulse characteristics per pass through a discrete element with transfer functions that can be expressed as jump conditions on the pulse parameters $[P_{\mathrm{i}},\tau_{\mathrm{i}},C_{\mathrm{i}}]\rightarrow[P_{\mathrm{f}},\tau_{\mathrm{f}},C_{\mathrm{f}}]$, where the subscript "i" ("f") represents input (output) parameter values. Here we will describe such transfer functions for the Gaussian *ansatz* (5.11) considered previously for fiber propagation. To model the saturable absorber, we will assume we are in the limit where the transfer function (5.6) is valid. To see how the pulse parameters change we approximate the function:

$$\left[1-\frac{q_0}{1+\dfrac{P_{\mathrm{i}}}{P_{\mathrm{s,A}}}\mathrm{e}^{-\frac{t^2}{\tau_{\mathrm{i}}^2}}}\right]\sqrt{P_{\mathrm{i}}}\mathrm{e}^{-(1-\mathrm{i}C_{\mathrm{i}})\frac{t^2}{2\tau_{\mathrm{i}}^2}}\sim\sqrt{P_{\mathrm{f}}}\mathrm{e}^{-(1-\mathrm{i}C_{\mathrm{f}})\frac{t^2}{2\tau_{\mathrm{f}}^2}} \tag{5.14}$$

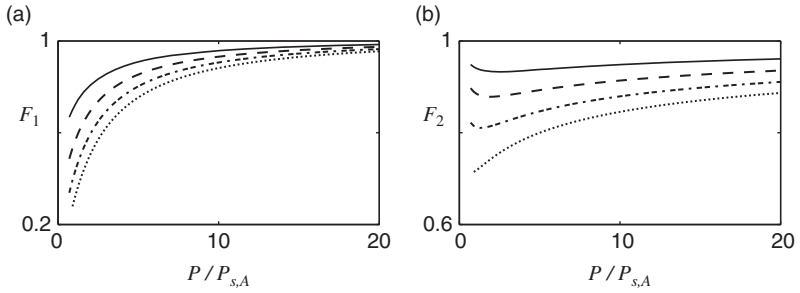

Figure 5.4 (a) Peak power and (b) pulse duration response (5.15) of the discrete saturable absorber for $q_0 = 0.3$ (——), 0.5 (– – –), 0.7 (–·–·–), and 0.9 (····).

Using a linear least-squares fitting routine, we numerically find that the parameters can be mapped using the functions:

$$P_\mathrm{f}/P_\mathrm{i} = F_1(q_0, P_\mathrm{i}/P_\mathrm{s,A}), \quad \tau_f/\tau_i = F_2(q_0, P_\mathrm{i}/P_\mathrm{s,A}), \quad C_\mathrm{f}/C_\mathrm{i} = \tau_\mathrm{i}^2/\tau_\mathrm{f}^2 \tag{5.15}$$

where F_1 and F_2 are shown in Figure 5.4. The modulation of P_f is independent of the input pulse duration τ_i, where the output pulse duration depends linearly on the input duration. Further, under this approximation the saturable absorber is only an amplitude modulator and changes the chirp parameter only due to the change in pulse duration. The simple form of the output coupler (5.7) translates only to a scalar multiplication of the peak power:

$$P_\mathrm{f} = R \times P_\mathrm{i}. \tag{5.16}$$

In general the application of a discrete spectral filter will cause modulation in both the amplitude and phase parameters. Indeed, it can cause a significant change in the pulse shape depending on the particular shape and characteristics of the input pulse and filter. To gain insight into the action of the spectral filter on a pulse, we assume a Gaussian profile for the spectral filter $\hat{A}(\omega) = \exp\left[-\omega^2/(2\Omega_\mathrm{F}^2)\right]$ so that the integral (5.8) can be calculated analytically for a chirped Gaussian pulse (5.11). Taking the Fourier transform of (5.11), multiplying by $\hat{A}(\omega)$, and integrating, we obtain a Gaussian pulse with modified parameters [116]:

$$P_\mathrm{f} = \sqrt{\frac{1+C_\mathrm{i}^2}{a^2+C_\mathrm{i}^2}} \times P_\mathrm{i}, \quad \tau_\mathrm{f} = \sqrt{\frac{a^2+C_\mathrm{i}^2}{a(1+C_\mathrm{i}^2)}} \times \tau_\mathrm{i}, \quad C_\mathrm{f} = \frac{C_\mathrm{i}}{a}, \quad \Omega_\mathrm{f}^2 = \frac{\Omega_\mathrm{i}^2}{a} \tag{5.17}$$

where $\Omega_\mathrm{i}^2 = (1+C_\mathrm{i}^2)/(2\tau_\mathrm{i}^2)$ and $a = 1 + 2\Omega_\mathrm{i}^2/\Omega_\mathrm{F}^2$. Note that as $\Omega_\mathrm{F} \to \infty$, $a \to 1$, resulting in no modification of the pulse parameters. If the filter bandwidth is less than or comparable to the pulse bandwidth ($1 < a$), the action of the spectral filter will reduce the pulse bandwidth by a factor of $1/\sqrt{a}$. Further, for highly chirped input pulses where $C_\mathrm{i} \gg 1$, the action of the spectral filter also reduces the pulse duration

Color Fig.: 5.5

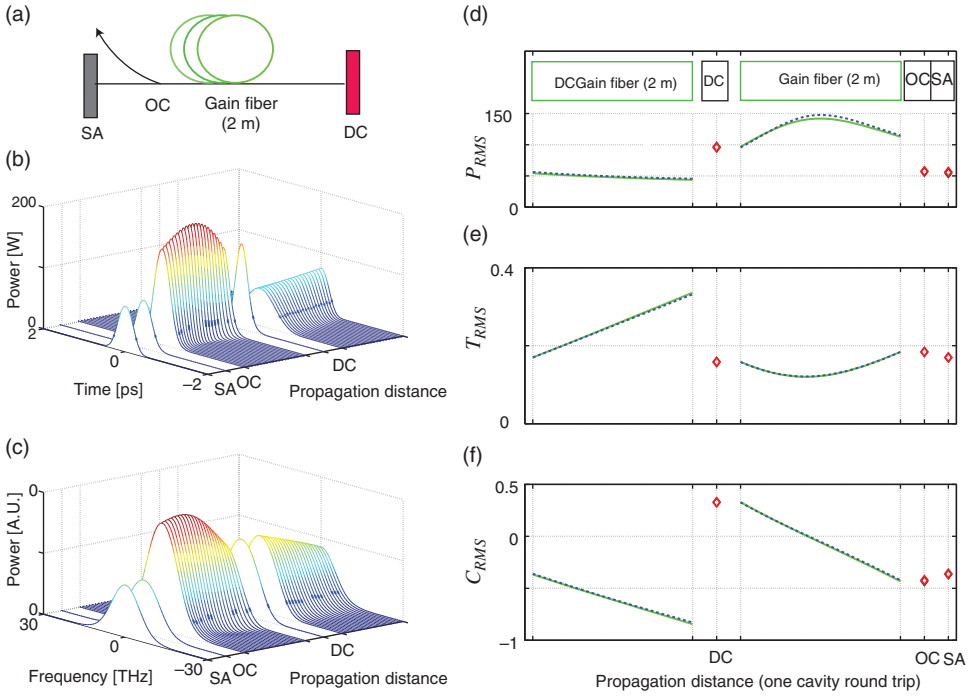

Figure 5.5 (a) Laser set-up. SA, saturable absorber; OC, output coupler; DC, dispersion compensator. Steady state (b) temporal and (c) spectral power from numerical simulation of Equations 5.1 and 5.3 with discrete actions [(5.6), (5.7)] with parameters: $\beta_2 = 0.02$, $\eta = 0.005$, the gain fiber is 2 m long, $g_0 = 3\log(10)$ (corresponding to 30 dB gain), $P_{s,g} \times T_R = 1$, $\Omega_g = 10$, $q_0 = 0.7$, $P_{s,A} = 3$, $R = 0.5$, total dispersion provided by DC $= 0.085$ ps^2. RMS (d) power (W), (e) duration (ps), and (f) chirp parameter (THz^{-2}) found from Equations 5.1 and 5.3 with discrete actions Equations 5.6 and 5.7 (green lines, black diamonds – the black diamonds are overlapped by the red diamonds defined below) compared with that found from the reduced model Equations 5.12 and 5.13 with discrete transfer functions Equations 5.15 and 5.16 (dashed, red diamonds) over one cavity round trip once steady state evolution is achieved.

Q7

by the same factor. This is a similar action to that of an anomalous dispersion fiber for dispersion compensation.

To show that the reduced model is valid, we consider a linear Yb-doped fiber laser configuration as depicted in Figure 5.5a. The laser consists of a saturable absorber (SA) and dispersion compensator (DC) at each end of the resonator. The operating wavelength is assumed to be where the dispersion of the gain fiber is in the normal regime, thus the discrete DC component provides anomalous dispersion. The output coupler is placed just before the saturable absorber after two passes through the gain fiber per round trip. This laser set-up is similar to experimental designs that will be shown in Section 5.3. Figure 5.5b and c show the steady state pulse dynamics over one cavity round trip found from numerical simulations. Here pulse propagation in the gain fiber is given by Equations 5.1 and 5.3. The DC component is found by solving

Equations 5.1 and 5.3 with $\gamma = g_0 = 0$. The SA and OC component is found by solving Equations 5.6 and 5.7 respectively. A comparison of the pulse parameters at steady state obtained from the full numerical simulation in Figure 5.5b and c with those obtained by solving the reduced system (5.12)–(5.13) and discrete operations (5.15)–(5.16) is shown in Figure 5.5d–f. The initial condition for the full simulation is initial white noise of intensity ~ 0.01 and for the reduced model was $[P, \tau, C] = [0.01, 5, 0]$. Clearly, from Figure 5.5d–f the dispersion compensator causes the chirp value to go through a zero point, leading to breathing dynamics in the pulse similar to stretched pulse operation. Both the dispersion compensator and the output coupler cause large changes in the pulse parameters, thus an averaged model would not capture the involved pulse dynamics shown here. The diamonds from both full simulation and the reduced model are overlapped and on the scale shown are difficult to distinguish. The solution of the reduced model does not have any long-scale oscillations, and it is remarkable how accurately the reduced model represents the full equation dynamics (to within $\sim$0.5%).

Although the reduced model equations do an excellent job of modeling certain dynamics and properties of pulse solutions in ultrafast lasers, there are some inherent limitations in such a scheme. Many modern lasers show pulse solutions that not only have evolving parameters in the cavity, but also have evolving temporal and spectral shapes [92–94]. Once a particular functional form is chosen in the reduced model, these structural changes cannot be predicted. However, interestingly, these structural changes will only change the coefficients in the model, and the overall trends in the pulse parameters are still well represented even when the pulse structure changes within one cavity round trip. Another limitation comes from the fact that we are assuming a single pulse solution with RMS quantities defined in (5.9). Thus, phenomena such as multipulsing or bi-stability cannot be captured. Although it is important to be aware of these limitations, the accuracy typically observed from the reduced model in characterizing the pulse evolution allows one to model such complex laser systems at a reduced computational price. In the next subsection we discuss how this can be used for optimization for varying system and design parameters.

5.2.4
Numerical Optimization of Laser Systems

As we have seen in our model equations, there are many system parameters to consider when optimizing a mode-locked fiber laser. In addition to system parameters, the actual laser set-up can be engineered efficiently so as to obtain the desired pulse characteristics. Optimizing over such system parameters and potential set-ups with full numerical simulations Equations 5.1–5.8 is a highly costly computational task [117]. To simplify this computation, the reduced equations (5.12)–(5.13) along with scalar transfer functions (5.15)–(5.17) can be used (under the limits in which they are valid). Per cavity round trip, the reduced system requires solving the (3×3) system (5.12) followed by M scalar multiplications for the M discrete elements. In contrast, simulations of the full equations (5.1)–(5.3) involve solving an $(N \times N)$

Color Fig.: 5.6

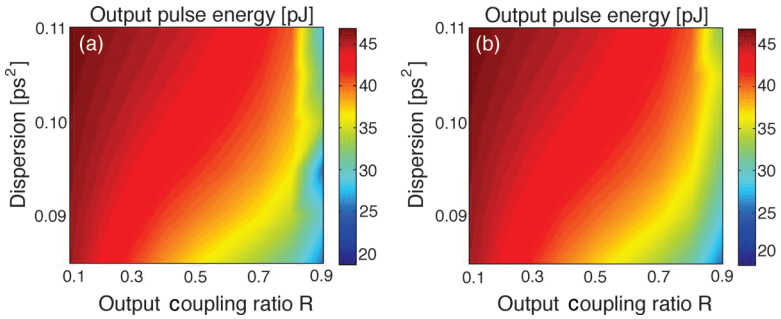

Figure 5.6 Output pulse energy of the laser set-up in Figure 5.5 with variable output coupling ratios R and varying dispersion provided by the DC component. Pulse energies obtained from simulations of (a) full equations (5.1) and (5.3) along with (5.6) and (5.7) and (b) reduced equations (5.12) and (5.13) along with (5.15) and (5.16).

system (N large) after discretization, plus M discrete transfer function multiplications. Thus, using the reduced model can allow for a wide range of parameter space to be explored at a fraction of the computational cost. To give a specific example, we optimize the output pulse energy of the linear laser configuration shown in Figure 5.5a when the output coupling ratio and the cumulative dispersion of the cavity is changed. The cumulative dispersion is varied by changing the dispersion of the DC component. Figure 5.6 shows the pulse energy obtained from both numerical simulations of the full equations (5.1) and (5.3) along with (5.6)–(5.7) and that of the reduced equations (5.12)–(5.13) along with (5.15)–(5.16). To obtain this figure, the relevant equations were numerically solved per cavity round trip with the parameters described in Figure 5.5 but with $R \in (0.1, 0.9)$ (increments of 0.1) and the dispersion from the DC component is $\in (0.097, 0.102)$ ps^2, giving the total dispersion provided for the cavity a range from $\in (-0.022, -0.017)$ ps^2 (increments of 0.001). Thus there was a total of $9 \times 6 = 54$ simulations. Each simulation was continued until the 2-norm of the vector:

$$\vec{Q} = \sqrt{\left[\vec{P}^{n+1}_{\mathrm{RMS}} - \vec{P}^{n}_{\mathrm{RMS}}\right]^2 + \left[\vec{T}^{n+1}_{\mathrm{RMS}} - \vec{T}^{n}_{\mathrm{RMS}}\right]^2 + \left[\vec{C}^{n+1}_{\mathrm{RMS}} - \vec{C}^{n}_{\mathrm{RMS}}\right]^2} \tag{5.18}$$

was within a certain tolerance ($= 0.001$). In Equation 5.18 each RMS vector represents the RMS values over one cavity round trip, where n denotes the round trip number. The initial condition for the full model is white noise of intensity ~ 0.01, and for the reduced model is $[P, \tau, C] = [0.01, 5, 0]$. On a standard personal computer, the amount of computational time needed to solve the full system of equations for all 56 simulations was $\sim$6 h when the number of modes was $N = 2^{10}$. The solution converged within an average of 52 round trips. In contrast, the reduced model is independent of the number of modes N and was able to provide the results shown in Figure 5.6 in 42 min with convergence obtained within an average of 32 round trips. Figure 5.6 shows that the reduced model does an excellent job in describing the laser system, and its significantly reduced computational time can be further exploited.

Color Fig.: 5.7

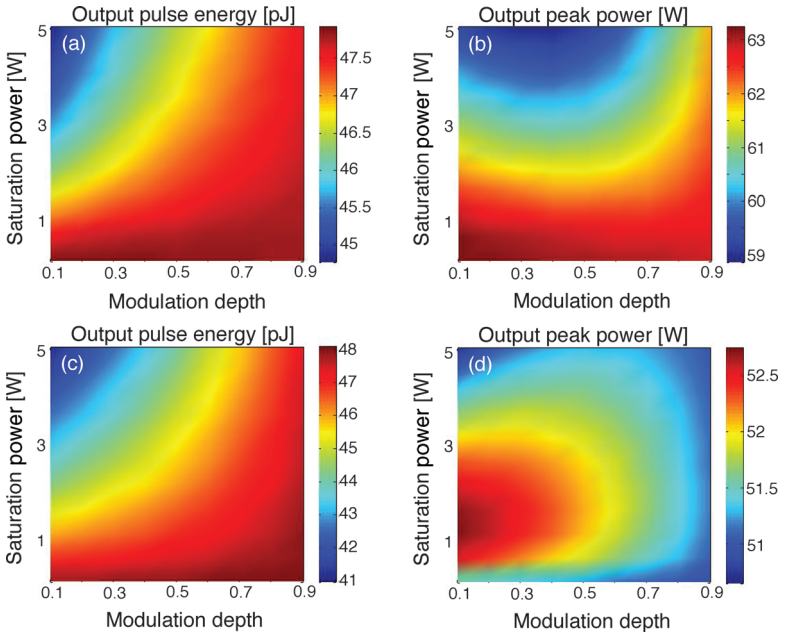

Figure 5.7 Output pulse energy and power from [(a), (b)] the laser set-up in Figure 5.5a and [(c), (d)] modified scheme similar to that in Figure 5.5a but with the output coupler before the DC component. The pulse characteristics were found from the reduced equations (5.12) and (5.13) along with (5.15) and (5.16) and all parameters are the same as in Figure 5.5 but with $R = 0.1$ and the total dispersion from the DC component is 0.1 ps^2.

As we can see from Figure 5.6, the value of the dispersion provided by the DC component as well as the output coupling ratio are key in determining the optimal output energy for a given saturable absorber. Specifically, higher values of anomalous dispersion and higher values of output coupling ratio $(1-R)$ provide the highest output pulse energies for this specific configuration. By using the reduced model, we can perform relatively quick parameter sweeps to optimize output pulse characteristics. Figure 5.7a and b shows the output pulse energies and peak powers obtained using the reduced model equations on the same configuration as shown in Figure 5.5a, but now for various saturable absorber parameters. We see here that the saturable absorber parameters do not play a huge role in increasing the pulse energy, and are less significant than the previously considered parameters of output coupling ratio and dispersion provided by the DC component. As a final example, the reduced model can be used not only with various parameter sweeps for a particular laser configuration but it can also easily be updated to consider changes in the configuration itself. Figure 5.7c–d shows the output energy and peak power for the laser configuration as in Figure 5.5a, but now with the output coupler just before the DC component. Similar to Figure 5.7a and b, we optimize over the modulation depth and power saturation parameters of the saturable absorber. Interestingly, in this configuration, although the pulse energies follow the same trend as in the

previously considered configuration, the peak power trend is slightly different. Indeed, comparing Figure 5.7b and d shows that higher peak powers are possible in the original configuration. Different behaviors from different set-ups are to be expected since mode-locked fiber lasers are nonlinear in nature, and so the order of operation is significant. Although here we have focused on optimizing pulse energies and peak powers, it is also possible to optimize other output pulse characteristics such as pulse duration, chirp value, or bandwidth.

In the following section we discuss some recent experimental advances in engineering SESAM parameters as well as mode-locked fiber lasers. The laser configurations considered are similar to that modeled in Figure 5.5a, and these systems were experimentally guided by the aforementioned numerical optimized schemes to obtain the desired output pulse characteristics.

5.3
Implementation and Control of Advanced Components

5.3.1
SESAM Engineering and Control

As discussed in the previous sections, a saturable absorber in the laser cavity can initiate pulsed laser operation from initial white noise. Ideally, this occurs from normal noise fluctuations, where one noise spike is strong enough to significantly reduce the saturable absorber loss and thus will be more strongly amplified during the following round trips, so that the stronger noise spike continues to further reduce its loss and continues its growth until it reaches steady state where a stable pulse train has been formed. As mentioned previously, there are key macroscopic quantities of saturable absorbers that are capable of characterizing the start-up dynamics of the mode-locked laser such as the modulation depth and recovery time [13]. In one study based on a Yb-doped fiber laser, SESAMs with small modulation depth resulted in self-starting only in the anomalous dispersion regime. However, when a large modulation depth absorber was used, self-starting mode-locking was achieved for both anomalous and normal dispersion cavities [118]. Furthermore, too short or too long an absorber recovery time resulted in more cavity round trips necessary for mode-locked operation.

When considering the modulation depth and recovery time of the absorber, it is important to account for the modifications of such parameters due to the amount of background radiation caused by amplified spontaneous emission (ASE) from the gain medium. The background radiation and its effect on the saturable absorber can be analyzed based on the rate equation (5.4) [119]. When the optical field circulating inside the laser cavity contains a significant fraction of the ASE, the total field intensity can be expressed as a time-dependent optical pulse and a time-independent component P_{ASE} representing the background ASE radiation $|U_{\mathrm{i}}(t)|^2 = |U_{\mathrm{i}}(t)|^2 + P_{\mathrm{ASE}}$. Substituting this expression for the optical field in Equation 5.4 we obtain a modified rate equation that is identical but with modified modulation depths

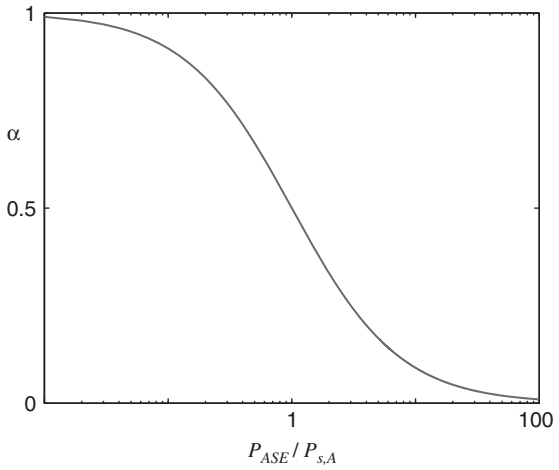

Figure 5.8 Modified coefficient for the recovery time and modulation depth of the saturable absorber model (5.4) due to amplified spontaneous emission of power level P_{ASE} in the laser cavity.

$q_0 \rightarrow \alpha q_0$ and recovery times $\tau_{\mathrm{A}} \rightarrow \alpha \tau_{\mathrm{A}}$, where $\alpha = 1/\left[1 + P_{\mathrm{ASE}}/P_{\mathrm{s,A}}\right]$. Figure 5.8 shows how α depends on the power ratio $P_{\mathrm{ASE}}/P_{\mathrm{s,A}}$ and illustrates that significant ASE can cause a reduction in both the modulation depth and recovery time, making start-up more difficult. In general, the modulation depth, start-up time, and amount of ASE level needs to be optimized for efficient start-up dynamics. Optimization of a particular saturable absorber should address the specific features of the laser. In this section we focus on SESAM engineering technologies and how certain key parameters can be controlled and optimized to achieve a self-starting device for mode-locking fiber lasers.

General analysis of a mode-locked laser without GVD or SPM showed that mode-locking is possible with both fast and slow saturable absorbers, where fast (slow) is characterized by the response time of the absorber compared to the resultant pulse duration [120]. Typically, better pulse quality requires as fast a response time as possible; however, this can sacrifice self-starting capabilities as the fast absorber cannot provide sufficient pulse shaping. If the recovery time is too long, ASE saturates the absorber, leading to a decrease in the modulation depth that can also degrade the self-starting capability. A semiconductor absorbs light when the photon energy is sufficient to excite carriers from the valence band to the conduction band. Under conditions of strong excitation, the absorption is saturated because possible initial states of the pump transition are depleted while the final states are partially occupied. Within 60–300 fs of excitation, the carriers in each band thermalize, and this leads to a partial recovery of the absorption. On a longer time scale, typically between a few picoseconds and a few nanoseconds, the carrier will be removed by recombination and trapping. To provide efficient ultrashort pulse shaping, the saturable absorption should recover to its initial value in a range from sub-picosecond to a few tens of picoseconds, depending on gain medium and laser cavity [121]. The intrinsic recombination processes for typical epitaxially-grown compound

semiconductors, in particular multiple-quantum-well structures, are usually too slow. Therefore, SESAM fabrication usually includes special measures to generate defect states in the band gap, which gives rise to fast carrier trapping to deplete the bands and reduce the recovery time. It is possible to reduce the response time by using special growth techniques or by using post-growth fabrication. Low temperature growth is very efficient in reducing the recovery time of GaAs-based devices [122]; however, it usually produces a non-uniform distribution of the recovery time over the sample. Another method is based on the growth-controlled crystalline quality of multiple-layer heterostructures using lattice mismatch induced non-radiative recombination centers [123]. To introduce and control the number of the non-radiative centers in the absorbing region, a buffer "lattice reformation" layer is grown between the DBR and absorber. Lattice-mismatching of the buffer layer is instrumental in introducing non-radiative centers and results in reducing the recovery time by trapping optically excited carriers into defect states, for example, misfit dislocations. The lattice reformation layer controls the density of the non-radiative centers in the absorber region formed on the reformation layer. This technique can exploit a large variety of semiconductor material systems with low and large lattice mismatches; however, a high value of non-radiative centers can result in high excess loss, preventing self-starting. In addition to growth techniques to reduce the response time, there are also post-growth treatments, including proton bombardment [124], and ion irradiation [125].

As an example of how the recovery time can be reduced by ion implantation, Figure 5.9 shows the carrier lifetimes for a layer structure containing 5 GaInAs/GaAs quantum wells at 1.1 μm as a function of 10 MeV Ni^{3+} dose. The lifetime is reduced by a factor of 500, as the ion dose is increased from 1×1010 to 50×1010 ion cm^{-2}, enabling sub-picosecond pulse durations ($\sim$ 600 fs), as deduced from decay times of time-resolved photoluminescence (TRPL). Post-implantation annealing at 610 °C for

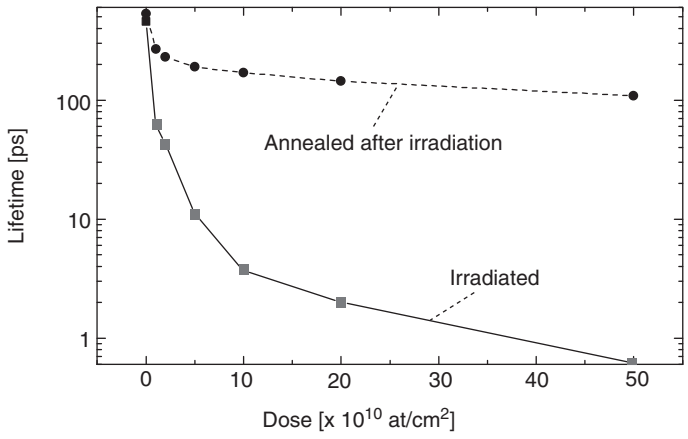

Figure 5.9 Carrier lifetime of a 1.1 μm SESAM equipped with five 6-nm wide GaInAs/GaAs quantum wells as a function of a dose of 10-MeV Ni^{3+} ion irradiation before and after annealing (610 °C for 1 min). The speed of SESAM can be controlled by ion implantation.

1 min improves the crystalline lattice and increases the recovery time. At shorter wavelengths of 0.94 μm, Ni^{3+} irradiation (50×1010 ions cm^{-2}) can yield 1 ps recovery times, which are two orders of magnitude shorter than the recovery time of the grown absorber [126]. In general, ion irradiation is a simple method but can pose certain problems due to its low reproducibility and uniformity. The long penetration depth of the ions can lead to structural degradation of the semiconductor mirror and results in an increase of the non-saturable loss [126]. Although proton bombardment was shown to reduce the recovery time down to 1 ps, the recombination centers created have low activation energies that may lead to long-term instabilities induced under exposure to intense optical radiation. Typically, post-growth fabrication, including proton bombardment and ion implantation, requires steps using expensive equipment.

As discussed previously, a large modulation depth for the absorber increases the probability for self-starting mode-locking, especially with large dispersion in the cavity. A resonant absorber, as opposed to the non-resonant absorbers previously discussed, is made by coating the surface with a reflecting layer consisting of a pair of $\lambda/4n$ dielectrics or a metallic thin-film and can typically have a larger modulation depth. It is interesting to ask the question as to whether fabrication techniques to modify the response time will influence the other properties, including the modulation depth, of the absorber. Figure 5.10a shows the nonlinear reflectivity from experiments in which the recovery time of the InGaAs quantum-well absorption was reduced by two orders of magnitude using heavy-ion irradiation of 10-MeV nickel ions [119]. The saturation fluence increased from 3.3 to 5.0 μJ cm^{-2} while the modulation depth decreased from 18.3 to 17.7, showing that the post-fabrication process did not have much of an effect on these parameters. However, the non-saturable losses increased from 8 to 16 after ion radiation, but still they are tolerable in a fiber laser cavity. Figure 5.10b shows the effective modulation depth as a function of incident CW-radiation for both SESAMs. For the as-grown slow absorber, the incident

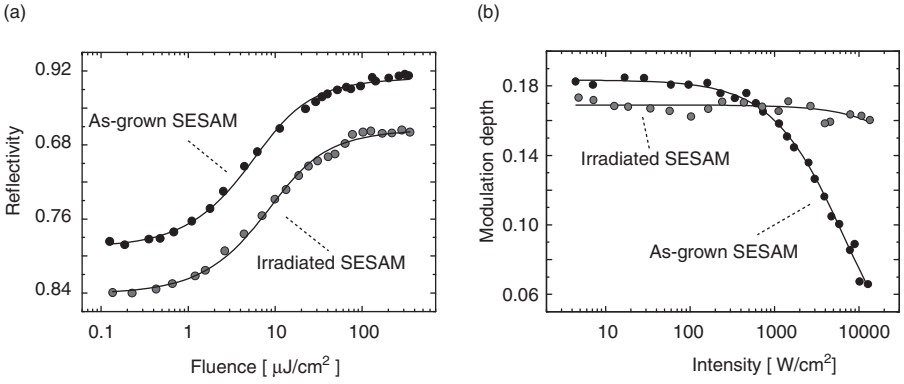

Figure 5.10 Experimentally measured (a) nonlinear reflectivity change for various pulse energy densities and (b) effective modulation depth for various levels of CW radiation of the absorber mirror before and after heavy-ion irradiation.

CW-light degrades the modulation depth. Remarkably, with an intensity of 10000 $W\,cm^{-2}$, corresponding to a CW-power level of 3 mW, the effective modulation depth decreases by ~70%, where the post-treated sample only decreases by ~1%. Thus, in the case highlighted here the post-treatment or special growth techniques do not significantly change the other key properties of the absorber [119].

5.3.2 Example of Dispersion Management in Mode-Locked Fiber Lasers Based on Chirped Fiber Bragg Gratings

As discussed previously, a CFBG is a type of distributed Bragg reflector that is achieved by adding a linear variation (or chirp) in the periodic structure of the refractive index of the fiber core. This sub-structure in the index profile not only makes the CFBG a wavelength-specific reflector, but also adds dispersion to the reflected field, since different wavelengths reflected from the grating will be subject to different delays [17]. Depending on whether the slope of the linear variation in the grating period is positive or negative, the CFBG can provide anomalous or normal dispersion. The total second order dispersion generated by the CFBG is given by $\beta_2 = n\lambda_0^2 L_g/(\pi\Delta\lambda c^2)$, where n is the refractive index, λ_0 is the center wavelength of the signal, $\Delta\lambda$ is the grating bandwidth, L_g is the length of the grating and c is the speed of light. To give a specific example, the length of a CFBG would be 0.3 mm to compensate the dispersion in a typical fiber laser consisting of 5 m of standard optical fiber operating at $\lambda_0 = 1.05$ nm ($\beta_2 = 0.02$ $ps^2\,m^{-1}$) supporting sub-picosecond pulses with bandwidths of 20 nm ($\Delta\lambda = 20$ nm). To achieve the necessary grating bandwidth for such a short length of fiber, the grating should have a considerable chirp. However, increasing the chirp parameter decreases the reflectivity power, thus it is necessary to optimize the grating for optimal dispersion compensation and reflectivity. In the following subsections we discuss two different mode-locked fiber lasers that use CFBG as dispersion compensators to provide anomalous dispersion in a ytterbium-doped fiber laser operating around 1 μm and normal dispersion in a thulium/holmium fiber laser operating around 2 μm.

5.3.2.1 Dispersion Management Using CFBG in a Ytterbium-Doped Mode-Locked Fiber Laser

Figure 5.11 shows the Yb-doped all-fiber laser setup [127], where the gain is provided by 1.5-m long Yb-doped fiber with 400 dB m^{-1} absorption at 976 nm. Note that this set-up is similar to that simulated and optimized in Figure 5.5. The doped fiber was pumped by a 976 nm semiconductor laser through a wavelength-division multiplexing (WDM) pump coupler. The operation wavelength is at 1060 nm so the fiber dispersion is in the normal GVD regime. This avoids soliton-like instabilities in fiber and allows for higher energy pulse outputs. One end of the linear cavity is terminated by a SESAM and the other by a CFBG. The CFBG used in this laser was 2.8 mm long with 170 nm cm^{-1} chirp and 50% reflectivity and provides anomalous dispersion of $\beta_2 = -0.39$ ps nm^{-1}. By observing the pulse at the various output ports 1–3 in Figure 5.11 the pulse duration, chirp, and spectrum change are seen along the cavity.

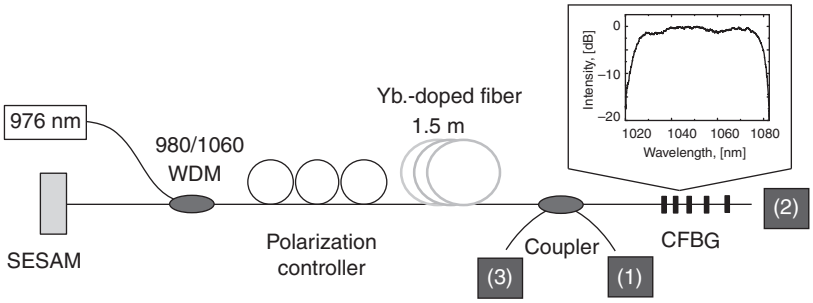

Figure 5.11 Experimental set-up of Yb-doped mode-locked fiber laser. Note that the output can be detected at various points in the cavity (1)–(3). Inset: reflection spectrum of a 2.8-mm long CFBG with 170 nm cm^{-1} chirp and 50% reflectivity.

Specifically, the pulses at the outputs "1" and "2" have positive chirp (up-chirped) where the pulses reflected from the grating to output "3" have negative chirp (down-chirped). This is easily explained since pulses propagating in the normal dispersion fiber will obtain a positive chirp, which is then compensated and turned negative by the dispersion of the CFBG upon reflection. The chirp allows for external compression of the optical pulse, and can lead to a transform-limited pulse. Compression of the down-chirped pulses from output port "3" requires a component with normal dispersion at the operation wavelength of 1.05 μm, which naturally suggests the use of standard single-mode fiber. A complete dechirping is observed for a 5.7-m length fiber (external to the cavity) leading to 126-fs transform-limited pulses with a time-bandwidth product of 0.41 (Figure 5.12a). Compression of the up-chirped pulse from output port "1" or "2" is more complicated, since it is necessary to provide anomalous dispersion at the operation wavelength of 1.05 μm. Here we show that this can be achieved using microstructured suspended-core fiber with a 2.7 μm diameter core

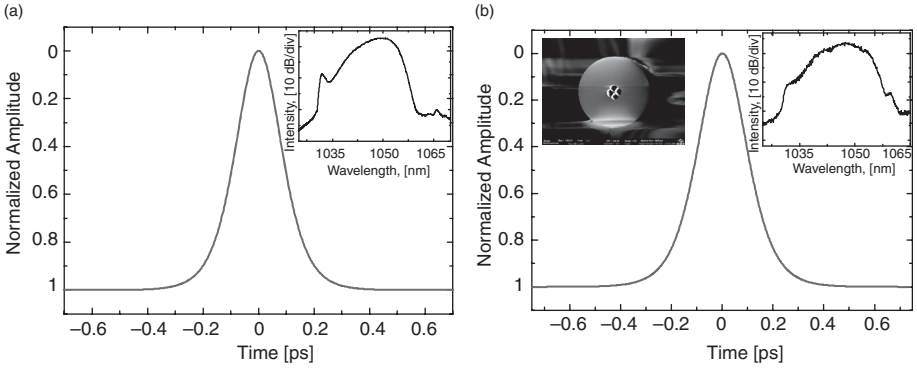

Figure 5.12 Autocorrelation and spectrum (inset) after compression of the output pulse from (a) port "3" (Figure 5.11) resulting in 126-fs transform-limited pulses and (b) port "2" resulting in 148-fs pulses. In (a) compression was carried out using standard fiber and in (b) it was performed with a SCF with cladding diameter of 100 μm (SEM image shown in inset).

surrounded by four holes, each with a size of 9.2 μm. The fiber exhibits an anomalous dispersion of 93 ps nm^{-1} km^{-1} at 1.05 μm. Compression of the down-chirped pulses from output port "2" by using 4.5 m of SCF gives 148-fs pulses with a 0.48 time-bandwidth product as shown in Figure 5.12b. A SEM image of the SCF cross section is shown in the inset. Although using a SCF can provide the necessary anomalous dispersion, pulse quality may be sacrificed due to the typically large value of third-order dispersion in the SCF. The total cavity dispersion can be adjusted by changing the length of the gain fiber. As an alternative to using external compression methods, it is also possible to obtain transform-limited pulses at the output ports by varying the total cavity dispersion by changing the length of the doped fiber [127]. It was found, for instance, that for a cavity length of 4.64 m, corresponding to a total cavity dispersion of 0.02 ps nm^{-1}, 1-ps pulses with a spectral bandwidth of 11 nm were obtained from output port "1." In general, since the pulse is breathing within the cavity, changing certain components will certainly effect the pulse output and the breathing dynamics can be used to optimize the output characteristics.

5.3.2.2 Dispersion Management Using CFBG in a Thulium/Holmium-Doped Mode-Locked Fiber Laser

In addition to the previously described Yb-doped fiber laser, numerous applications require high-energy pulses at an operation wavelength shifted towards the mid-infrared range. Here we investigate the use of thulium- and thulium–holmium-doped fibers in a mode-locked laser. Thulium-doped fiber has a broad amplification bandwidth between 1.65 and 2.1 μm and is, therefore, suitable for short pulse generation and wide spectral tuning. Typically for lasers requiring larger pulse energies, anomalous segments of fiber are minimized or eliminated altogether in the cavity. However, this requirement becomes increasingly difficult to fulfill for longer wavelengths due to limited availability of fibers with normal dispersion. Standard optical fiber operating at 2 μm has large anomalous dispersion, and thus pulse propagation in standard fiber is susceptible to soliton-like instabilities. To avoid such instabilities, a dispersion map is used in a thulium–holmium doped fiber laser where the normal dispersion is provided by a CFBG [128]. The laser set-up is similar to Figure 5.11, with the output ports "1" and "3" removed (the output was only taken at the CFBG). The Tm–Ho-doped gain fiber is 1.2 m long with absorption of 14 dB m^{-1} at 1564 nm and anomalous dispersion of 0.13 ps^2 m^{-1} at 1985 nm. The CFBG used in this laser was 4 mm long with 130 nm cm^{-1} chirp, $\sim$ 30% reflectivity, a bandwidth of 82 nm centered at 1986 nm, and provides normal dispersion of $\beta_2 = 1.07$ ps^2. Thus, the dispersion map of the cavity consisted of the gain segment with anomalous dispersion and a CFBG providing normal dispersion. By changing the length of the passive fiber, the net cavity dispersion could be either normal or anomalous in a range from 0.47 to -0.32 ps^2. Depending on the net dispersion various types of pulse characterizations are observed at the output. Figure 5.13a shows a typical spectral profile when the CFBG provides more than enough dispersion to compensate the fiber dispersion. In this example the cavity length was 4.5 m corresponding to the repetition rate of 22.7 MHz, bandwidth of 5 nm, and central wavelength of 1987 nm, as seen from Figure 5.13a. The pulse duration is 11.7 ps and is strongly up-chirped,

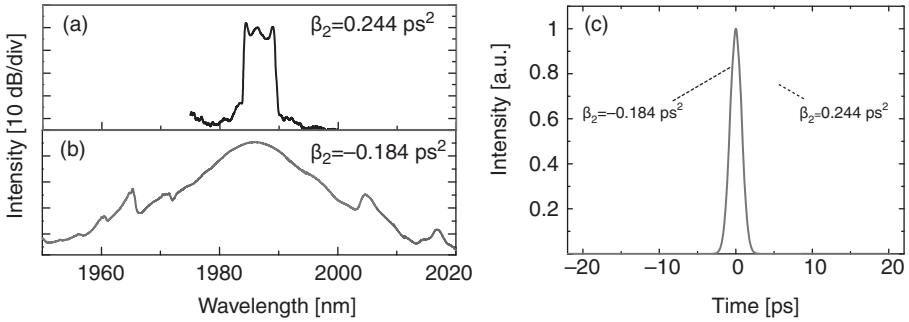

Figure 5.13 Typical spectral profiles of the output pulse when the net dispersion is (a) positive and (b) negative; (c) the autocorrelations of the pulses shown in (a) and (b).

corresponding to a time-bandwidth product of 15.69 (Figure 5.13c). When the net dispersion was normal, the single-pulse regime was maintained over the whole range of pump power, with the average output power limited to 50 mW at a pump power of 470 mW due to excessively large out-coupling provided by the CFBG. In contrast, Figure 5.13b shows a typical spectral profile when the CFBG does not provide enough dispersion to compensate the fiber dispersion. The spectrum bandwidth, pulse duration, and average power are 7.3 nm, 1.54 ps, and 20 mW, respectively. Multiple-pulse operation sets in with a minor increase in a pump power, as expected with typical DM soliton lasers. In general, the total length of the laser cavity was varied from 3 to 8.5 m, changing the repetition rate in a range of 12.2 to 33.3 MHz. When the laser operates in the net-normal GVD regime, the pulse has steep spectral edges, which are a signature of so-called dissipative solitons in the normal GVD regime. As the normal GVD decreases, the spectrum bandwidth increases. When the laser operates in the net-anomalous GVD regime, the spectra exhibit distinct Kelly sidebands inherent to solitons in the anomalous GVD regime. The spectral bandwidth increases for decreasing dispersion. Self-starting of the laser was achieved regardless of the sign or value of GVD owing to high modulation depth of saturable absorber. This particular dispersion management allows for various types of pulse solutions operating around 2 μm, with the potential to achieve higher energies when the CFBG provides enough normal dispersion to compensate the inherently large fiber dispersion at the operating wavelength.

5.3.3
Examples of Dispersion Management in Mode-Locked Fiber Lasers Based on Photonic Bandgap Fibers

As discussed in Section 5.1, microstructured fibers offer a substantial design freedom, allowing for different dispersion characteristics from fused silica [18, 19]. A microstructured fiber is an optical fiber that obtains its waveguide properties not from a spatially varying glass composition but from an arrangement of very tiny and closely spaced air holes that go through the whole length of the fiber. Solid-core

index-guided photonic crystal fiber (PCF) typically has a triangular pattern of air holes, with one hole missing. The guiding properties of this type of PCF can be roughly understood with an effective index model: the region with the missing hole has a higher effective refractive index, similar to the core in a conventional fiber. Indeed, they can have a much higher effective refractive index contrast between core and cladding, and can therefore have a much stronger confinement, increasing the nonlinearity of the fiber. In photonic bandgap fibers (PBG fibers) light is confined in a hollow core due to a photonic bandgap that arises from a regular two-dimensional array of air holes in the cladding. Unlike conventional optical fibers, PBG fibers do not guide light by total internal reflection but rely on a photonic bandgap in the fiber's cladding [129]. A hollow-core PBG fiber consists of a hollow core surrounded by a cladding whose periodicity creates a bandgap for the photons guided in the fiber's core. A hollow core fiber was first introduced in a mode-locked soliton laser operating at 1 μm to provide the necessary dispersion compensation [130], and has recently been studied for soliton propagation [131]. Although these fibers can be attractive for high-power soliton propagation, they can suffer from poor matching with standard fibers and, consequently, may generate high intracavity loss. Particularly in a mode-locked laser cavity, a hollow-core PBG fiber spliced with standard fiber could provide Fresnel back-reflection that is detrimental to self-starting.

An alternative to hollow core PBG fiber is solid-core PBG (SC-PBG) [132] fiber that is made with either a doped or undoped silica core and an array of Ge-doped elements or air holes in the cladding that confine the light in the core. Although the mode size in the SC-PBG fiber is typically slightly larger than the diameter of the mode field in the core of a standard fiber, there is typically good mode matching capability with standard fibers. When compared to ordinary index-guided fibers, SC-PBG fibers have anomalous GVD at shorter wavelengths. This property, along with the lower nonlinearity due to the larger mode diameter, makes SC-PBG fiber an excellent candidate to provide anomalous dispersion compensation while avoiding soliton-like instabilities in a high-energy ytterbium mode-locked fiber laser operating near 1 μm. Indeed, a SC-PBG fiber with an undoped core was used for dispersion compensation in a Yb mode-locked fiber laser self-started by a SESAM and operating at 1.04 μm [133]. Since the laser consists of sections of standard fiber with normal dispersion along with the SC-PBG with anomalous dispersion, the pulse duration and chirp evolve slightly per cavity round trip. The SC-PBG provides sufficient dispersion to make the net-dispersion anomalous, resulting in soliton-like pulses [133]. This laser was optimized by changing both the length of the active fiber (amount of normal dispersion) and the operation wavelength, giving the shortest pulse duration of 460 fs, with a spectral bandwidth of 4.6 nm. Since the time–bandwidth product (= 0.59) is still above the value of that of a transform limited pulse, it can potentially be able to be compressed further with some form of external compression. However, a major limitation in using the SC-PBG is its high value of third-order dispersion, which causes an asymmetry in the pulse spectrum, effectively limiting the amount of compression possible while not sacrificing pulse quality.

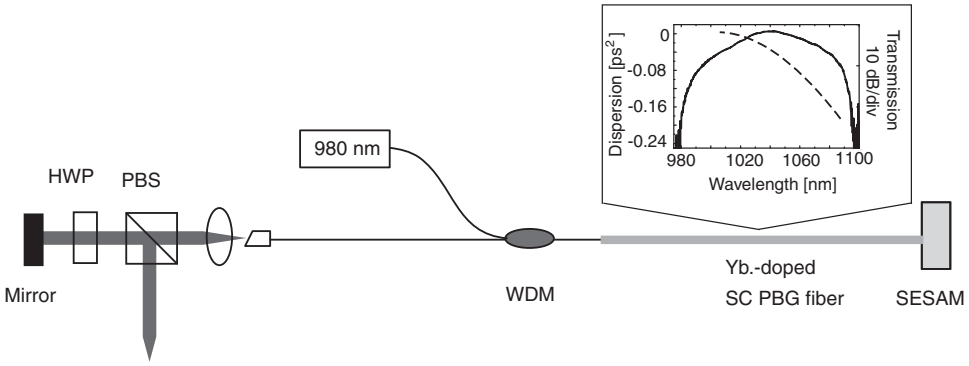

Figure 5.14 Laser setup with Yb-doped SC-PBG fiber. HWP: half-wave plate, PBS: polarizing beam splitter, WDM: wavelength-division multiplexing pump/signal. Inset: dispersion of the fiber cavity (– – –) and the transmission spectrum of the second-order bandgap of the Yb-PBG fiber (——).

Q8

In addition to their dispersion and nonlinearity properties, SC-PBG fibers also have the potential to have their cores doped with rare-earth ions. Er- and Yb-doped PCFs were first reported and have later been used in different types of lasers [134, 135] and amplifiers [136]. More recently, Nd-doped photonic crystal fiber has been used as gain medium in a passively mode-locked fiber laser at 1.06 μm [137]. Here we present a mode-locked laser using a ytterbium-doped photonic bandgap (Yb-PBG) fiber as both the gain medium and a dispersion compensator [138]. The experimental setup is illustrated in Figure 5.14. The fiber cavity consists of 0.27 m of Yb-doped SC-PBG fiber and 0.47 m of standard single mode fiber. The free end of the Yb-doped PBG fiber is butt-coupled directly to a SESAM. The laser output is taken from a variable coupler composed of a polarizing beam splitter and a half-wave plate placed in the free space section of the cavity. The output coupling was maximized by rotating the half-wave plate. Depending on the cavity parameters, the optimal value of the output coupling that allowed for stable mode-locked operation ranged from 0.2 to 0.5. The laser was pumped with a single-mode grating-stabilized laser diode capable of delivering up to 300 mW of power at 980 nm. The inset in Figure 5.14 shows the second-order transmission band of the Yb-doped SC-PBG fiber recorded using a white-light source. The bandgap ranges from 980 to 1100 nm, covering both the pump wavelength and the laser transition of the Yb-doped fiber. Although the transmission band shape of the PBG fiber is to a certain extent affected by the high level of Yb-doping, it is evident that the pump wavelength is located close to the short-wavelength edge of the band. The pump radiation is, therefore, weakly guided and may decrease the overall pump efficiency. Optimization of the spectral band positioning would potentially improve output power. The SC-PBG fiber has ten rings of Ge-doped inclusions with the refractive index of ~ 1.465 in a pure silica background surrounding the core. The fiber diameter is 200 μm and the periodic structure has a spacing of 8.3 μm. The core was formed by replacing one inclusion in the middle with a Yb-doped silica rod having a refractive index close to that of pure silica. The numerical aperture of the core is ~ 0.21 and it guides the fundamental

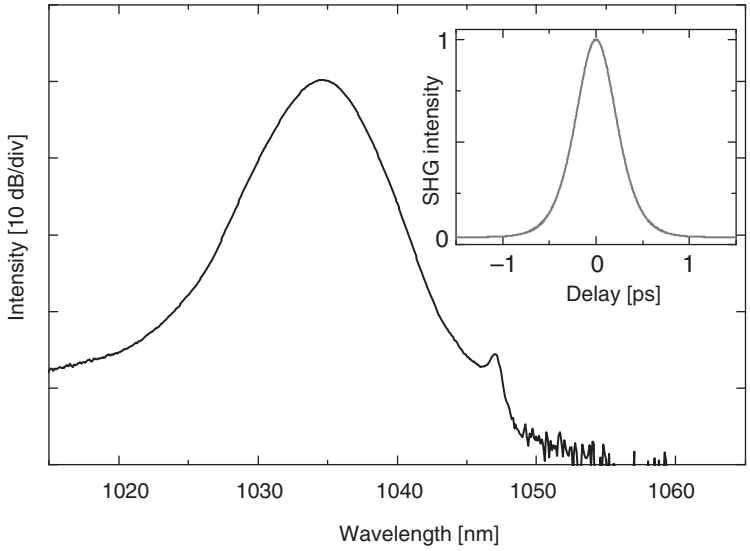

Figure 5.15 Mode-locked pulse spectrum from laser set-up shown in Figure 5.14. Inset: measured intensity autocorrelation. The output pulse has a FWHM bandwidth of 4 nm and pulse duration 335 fs.

mode with a field diameter of 9 μm. The mode size in the Yb-PBG fiber is slightly larger than the 6.4 μm mode diameter in the core of the standard fiber. Owing to small mode mismatch between bandgap fiber and normal fiber, the splice loss was ∼ 1 dB. The measured round-trip group-velocity dispersion (GVD) of the laser cavity is also shown in the inset of Figure 5.14. The dichroic pump coupler, made of standard single-mode fiber, has a normal GVD of $+0.024$ ps^2 m^{-1}, while the SC-PBG fiber exhibits anomalous GVD of -0.075 ps^2 m^{-1} at 1035 nm. Thus, the cavity has an anomalous round-trip dispersion of -0.017 ps^2 at 1035 nm, corresponding to the signal wavelength of the experiments. The laser was self-starting. Figure 5.15 shows the optical spectrum and corresponding intensity autocorrelation of the output pulse. The pulse bandwidth is ∼4 nm and a sech^2-fit to the intensity yields a pulse duration of 335 fs (FWHM), which gives a time-bandwidth product of 0.37, indicating a nearly transform limited pulse operation. Similar to the SC-PBG fiber with an un-doped core, a Yb-doped SC-PBG fiber exhibits significant third-order dispersion (TOD). For example, the TOD of the Yb-doped SC-PBG fiber in Figure 5.14 was estimated to be 2.3 ps^3 km^{-1} at 1.04 μm. This exceptionally large value of TOD was found to affect the shape of the pulse spectrum, causing notable asymmetry. Investigating this asymmetry by changing the length of both the standard single mode and Yb-doped SC-PBG fibers showed roughly 2–3 soliton sidebands in the long-wavelength tail (corresponding to higher anomalous dispersion regime), where sidebands were never recorded at the short-wavelength wing of the spectrum. Although the asymmetry can cause limitations in external compression, the higher order dispersion does not significantly restrict the ability to obtain mode-locking. In general, since the

dispersion compensation is provided by the gain fiber, simple and compact femtosecond laser architecture can be realized. This approach offers potentially higher repetition rates when compared with the previously described fiber lasers using standard Yb-doped fiber and a separate PBG fiber for dispersion compensation.

5.4 Conclusions and Future Outlook

Fiber lasers have a long history, starting with the proposal by Snitzer in 1961 [139] shortly after the seminal demonstration by Maiman of the ruby laser in 1960 [140]. Experimental demonstrations shortly followed in 1964 [141]. It took slightly more than two decades to develop the first commercial fiber lasers, which entered the market in the late 1980s. Nowadays fiber lasers present an excellent example of high-tech commercial devices that, at the same time, still belong to an ever-expanding field of active research. New ideas, concepts, and technologies constantly improve the performance of fiber-based laser systems and create new fields of applications. Ultrafast fiber laser systems have been actively studied over the last ten years, with a huge number of publications dedicated to the subject. This research has focused on the ability to expand the available operation parameters from such ultrashort sources. This rapid progress is based on a combination of four key factors:

1) Advances in material science have provided new gain media. More operation wavelengths are possible by implementing various rare-earth materials: erbium, ytterbium, neodymium, dysprosium, praseodymium, thulium, holmium, and bismuth.
2) Advances in material science have provided new non-artificial saturable absorbers such as SESAM technology as well as carbon-based saturable absorbers. Fabrication techniques currently developed allow for the control of both micro- and macroscopic properties of such devices.
3) Achievements in fiber optic design technology have led to fiber waveguides that allow for significant tailoring of fiber characteristics such as nonlinearity (from very low to very high) and dispersion. The production of microstructured fibers such as index-guided, photonic bandgap and holy fibers, as well as large mode area or multi-core fibers is now a mature technology that adds flexibility when considering dispersion and nonlinearity management.
4) The development of a fundamental understanding and control of the physical effects underlying the operation and performance of fiber lasers. Modern laser designs demand new theoretical descriptions since these systems support pulses that undergo large changes in their characteristics per cavity round trip. Novel pulse energy scaling approaches are possible using, among others, dissipative solitons and similariton propagation, and are free from limitations intrinsic to "classical" soliton systems.

Future progress along these lines will provide a basis for further progress in the field and a platform for the development of next-generation ultrafast fiber lasers.

Indeed, mode-locked fiber lasers are actively approaching the performance standards of solid-state lasers in several applications, making them viable candidates to replace them in the laboratory and commercial settings. Apart from numerous other advantages listed in this book, mode-locked fiber lasers have an inherent connection with telecommunication fiber technologies that provides a technical and economical basis for low-cost solutions. This gives ultrafast fiber lasers an important commercial edge, and is a reason why they represent the most viable user-friendly solution on the current market.

References

1 Jackson, S.D. (2009) The spectroscopic and energy transfer characteristics of rare earth ions used for silicate glass fibre lasers operating in the shortwave infrared. *Photonics Rev.*, **3**, 466–482.

2 Becker, P.C., Olsson, N.A., and Simpson, J.R. (1999) *Erbium-Doped Fiber Amplifiers: Fundamentals and Technology*, 1st edn, Academic Press, San Diego.

3 Desurvire, E., Bayart, D., Desthieux, B., and Bigo., S. (2002) *Erbium-Doped Fiber Amplifiers*, 1st edn, John Wiley & Sons Inc., New York.

4 Pask, H.M., Carman, R.J., Hanna, D.C., Tropper, A.C., Mackechnie, C.J., Barber, P.R., and Dawes, J.M. (1995) Ytterbium-doped silica fiber lasers: versatile sources for the 1–1.2 μm region. *IEEE J. Sel. Top. Quantum Electron.*, **1**, 2–13.

5 Paschotta, R., Nilsson, J., Tropper, A.C., and Hanna, D.C. (1997) Ytterbium-doped fiber amplifiers. *IEEE J. Quantum Electron.*, **33**, 1049–1056.

6 Cautaerts, V., Richardson, D.J., Paschotta, R., and Hanna, D.C. (1997) Stretched pulse Yb^{3+}: silica fiber laser. *Opt. Lett.*, **22**, 316–318.

7 Lefort, L., Price, J.H.V., Richardson, D.J., Spühler, G.J., Paschotta, R., Keller, U., Fry, A.R., and Weston, J. (2002) Practical low noise stretched-pulse Yb^{3+}-doped fiber laser. *Opt. Lett.*, **27**, 291–293.

8 Lim, H., Ilday, F.Ö., and Wise, F.W. (2003) Generation of 2-nj pulses from a femtosecond ytterbium fiber laser. *Opt. Lett.*, **28**, 660–662.

9 Okhotnikov, O.G., Gomes, L., Xiang, N., Jouhti, T., and Grudinin, A.B. (2003) Mode-locked ytterbium fiber laser tunable in the 980–1070-nm spectral range. *Opt. Lett.*, **28**, 1522–1524.

10 Moulton, P.F., Rines, G.A., Slobodtchikov, E.V., Wall, K.F., Firth, G., Samson, B., and Carter, A.L.G. (2009) Tm-doped fiber lasers: fundamentals and power scaling. *IEEE J. Sel. Top. Quantum Electron.*, **15**, 85–92.

11 Nelson, L.E., Ippen, E.P., and Haus., H.A. (1995) Broadly tunable sub-500fs pulses from an additive-pulse mode-locked thulium-doped fiber ring laser. *Appl. Phys. Lett.*, **67**, 19–21.

12 Sharp, R.C., Spock, D.E., Pan, N., and Elliot, J. (1996) 190-fs passively mode-locked thulium fiber laser with a low threshold. *Opt. Lett.*, **21**, 881–883.

13 Keller, U. (2007) Short and ultrashort pulse generation, in *Landolt-Börnstein, Group VIII/1B1, Laser Physics and Applications. Subvolume B: Laser Systems. Part I* (eds G. Herziger, H. Weber, and R. Proprawe), Springer Verlag, pp. 33–167.

14 Nyushkov, B.N., Denisov, V.I., Kobtsev, S.M., Pivtsov, V.S., Kolyada, N.A., Ivanenko, A.V., and Turitsyn., S.K. (2010) Generation of 1.7-microjoule pulses at 1.55 micron by a self-mode-locked all-fiber laser with a kilometers-long linear-ring cavity. *Laser Phys. Lett.*, **7**, 661–665.

15 Bennion, I., Williams, J.A.R., Zhang, L., Sugden, K., and Doran, N.J. (1996) Uv-written in-fibre Bragg gratings. *Opt. Quantum Electron.*, **28**, 93–135.

16 Hill, K.O. and Meltz, G. (1997) Fiber Bragg grating technology - fundamentals

and overview. *J. Lightwave Technol.*, **15**, 1263–1276.
17 Oulette, F. (1987) Dispersion cancelation using linearly chirped Bragg grating filters in optical waveguides. *Opt. Lett.*, **12**, 847–849.
18 Knight, J.C. (2003) Photonic crystal fibres. *Nature*, **424**, 847–851.
19 Russell, P.St.J. (2003) Photonic crystal fibres. *Science*, **299**, 358–362.
20 Spence, D.E., Kean, P.N., and Sibbett, W. (1991) 60-fsec pulse generation from a self-mode-locked Ti:sapphire laser. *Opt. Lett.*, **16**, 42–44.
21 Stolen, R.H., Botineau, J., and Ashkin, A. (1982) Intensity discrimination of optical pulses with birefringent fibers. *Opt. Lett.*, **7**, 512–514.
22 Doran, N.J. and Wood, D. (1988) Nonlinear-optical loop mirror. *Opt. Lett.*, **13**, 56–58.
23 Keller, U., Miller, D.A.B., Boyd, G.D., Chiu, T.H., Ferguson, J.F., and Asom, M.T. (1992) Solid-state low-loss intracavity saturable absorber for Nd:YLF lasers: an antiresonant semi-conductor Fabry–Perot saturable absorber. *Opt. Lett.*, **17**, 505–507.
24 Keller, U., Weingarten, K.J., Kärtner, F.X., Kopf, D., Braun, B., Jung, I.D., Fluck, R., Hönninger, C., Matuschek, N., and Aus der Au, J. (1996) Semiconductor saturable absorber mirrors (sesams) for femtosecond to nanosecond pulse generation in solid-state lasers. *IEEE J. Sel. Top. Quantum Electron.*, **2**, 435–453.
25 Keller, U. (1999) Semiconductor nonlinearities for solid-state laser mode-locking and q-switching, in *Nonlinear Optics in Semiconductors, Semiconductors and Semimetals*, vol. **59** (eds E. Garmire and A. Kost), Academic Press Inc., pp. 211–286.
26 Pashotta, R. and Keller., U. (2003) Ultrafast solid-state lasers, in *Ultrafast lasers: Technology and Applications* (eds M.E. Fermann, A. Galvanauskas, and G. Sucha), Marcel Dekker Inc., pp. 1–60.
27 Guina, M., Xiang, N., Vainionpää, A., Okhotnikov, O.G., Sajavaara, T., and Keinonen, J. (2001) Self-starting stretched-pulse fiber laser mode locked and stabilized with slow and fast semiconductor saturable absorbers. *Opt. Lett.*, **26**, 1809–1811.
28 Guina, M., Xiang, N., and Okhotnikov, O.G. (2002) Stretched-pulse fiber lasers based on semiconductor saturable absorbers. *Appl. Phys. B*, **74**, S193–S200
29 Okhotnikov, O.G., Jouhti, T., Konttinen, J., Karirinne, S., and Pessa, M. (2003) 1.5 μm monolithic GaInNAs semiconductor saturable absorber mode-locking of an erbium fiber laser. *Opt. Lett.*, **28**, 364–366.
30 Garnache, A., Hoogland, S., Trooper, A.C., Gerard, J.M., Thierry-Mieg, V., and Roberts, J.S. (2001) OT Pico-second passively mode locked surface-emitting laser with self-assembled semiconductor quantum dot absorber, in CLEO/Europe-EQEC (postdeadline paper).
31 Rafailov, E.U., White, S.J., Lagatsky, A.A., Miller, A., Sibbett, W., Livshits, D.A., Zhukov, A.E., and Ustinov., V.M. (2004) Fast quantum-dot-based saturable absorber for passive mode-locking of solid-state lasers. *IEEE Photon. Technol. Lett.*, **16**, 2439–2441.
32 Herda, R., Okhotnikov, O.G., Rafailov, E.U., Sibbet, W., Crittenden, P., and Starodumov, A. (2006) Semiconductor quantum-dot saturable mode-locked fiber laser. *IEEE Photon. Technol. Lett.*, **18**, 157–159.
33 Lagatsky, A.A., Bain, F.M., Brown, C.T.A., Sibbett, W., Livshits, D.A., Erbert, G., and Rafailov, E.U. (2007) Low-loss quantum-dot-based saturable absorber for efficient femtosecond pulse generation. *Appl. Phys. Lett.*, **91**, 231111.
34 Aschwanden, A., Lorenser, D., Unold, H.J., Paschotta, R., Gini, E., and Keller, U. (2005) 2.1-W picosecond passively mode-locked external-cavity semiconductor laser. *Opt. Lett.*, **30**, 272–274.
35 OÕConnell, M.J., Bachilo, S.M., Huffman, C.B., Moore, V.C., Strano, M.S., Haroz, E.H., Rialon, K.L., Boul, P.J., Noon, W.H., Kittrell, C., Ma, J., Hauge, R.H., Weisman, R.B., and Smalley, R.E. (2002.) Band gap fluorescence from individual

single-walled carbon nanotubes. *Science*, **297**, 593–596.
36 Hasan, T., Sun, Z., Wang, F., Bonaccorso, F., Tan, P.H., Rozhin, A.G., and Ferrari, A.C. (2009) Nanotube-polymer composites for ultrafast photonics. *Adv. Mater.*, **21**, 3874–3899.
37 Kivistö, S., Hakulinen, T., Kaskela, A., Brown, D.P., Nasibulin, A.G., Kauppinen, E.I., Härkönen, A., and Okhotnikov, O.G. (2009) Carbon nanotube films for ultrafast broadband technology. *Opt. Express*, **17**, 2358–2363.
38 Tian, Y., Timmermans, M.Y., Kivistö, S., Nasibulin, A.G., Zhu, Z., Jiang, H., Okhotnikov, O.G., and Kauppinen, E.I. (2011) Tailoring the diameter of single-walled carbon nanotubes for optical applications. *Nano Res.*, **4**, 807–815.
39 Set, S.Y., Yaguchi, H., Tanaka, Y., and Jablonski, M. (2004) Laser mode locking using a saturable absorber incorporating carbon nanotubes. *J. Lightwave Technol.*, **22**, 51–56.
40 Kieu, K. and Wise, F.W. (2008) All-fiber normal-dispersion femtosecond laser. *Opt. Express*, **16**, 11453–11458.
41 Bonaccorso, F., Sun, Z., Hasan, T., and Ferrari, A.C. (2010) Graphene photonics and optoelectronics. *Nat. Photon.*, **4**, 611–622.
42 Bao, Q.L., Zhang, H., Wang, Y., Ni, Z.H., Shen, Z.X., Loh, K.P., and Tang, D.Y. (2009) Atomic layer graphene as saturable absorber for ultrafast pulsed laser. *Adv. Funct. Mater.*, **19**, 3077–3083.
43 Popa, D., Sun, Z., Torrisi, F., Hasan, T., Wang, F., and Ferrari, A.C. (2010) Sub 200fs pulse generation from a graphene mode-locked fiber laser. *Appl. Phys. Lett.*, **97**, 203106–203108.
44 Zhang, H., Tang, D., Knize, R.J., Zhao, L., Bao, Q., and Loh, K.P. (2010) Graphene mode locked, wavelength-tunable, dissipative soliton fiber laser. *Appl. Phys. Lett.*, **96**, 111112.
45 Haus, H.A. (1975) Theory of mode-locking with a fast saturable absorber. *J. Appl. Phys.*, **46** (7), 3049–3058.
46 Haus, H.A., Fujimoto, J.G., and Ippen, E.P. (1991) Structures for additive pulse mode-locking. *J. Opt. Soc. Am. B*, **8**, 2068–2076.
47 Haus, H.A. (2000) Mode-locking of lasers. *IEEE J. Sel. Top. Quantum Electron.*, **6**, 1173–1185.
48 Aranson, I.S. and Kramer, L. (2002) The world of the complex Ginzburg–Landau equation. *Rev. Mod. Phys.*, **74**, 99–143.
49 Akhmediev, N. and Ankiewicz, A. (2005) Dissipative solitons in the complex Ginzburg–Landau and Swift-Hohenberg equations, in *Dissipative Solitons, Lecture Notes in Physics*, vol. **661** (eds N. Akhmediev and A. Ankiewicz), Springer, Berlin-Heidelberg, pp. 1–17.
50 Podivilov, E. and Kalashnikov, V.L. (2005) Heavily-chirped solitary pulses in the normal dispersion region: new solutions of the cubic-quintic complex Ginzburg–Landau equation. *JETP Lett.*, **82**, 524–528.
51 Kutz, J.N. (2006) Mode-locked soliton lasers. *SIAM Rev.*, **48**, 629–678.
52 Nelson, L.E., Jones, D.J., Tamura, K., Haus, H.A., and Ippen, E.P. (1997) Ultrashort-pulse fiber ring lasers. *Appl. Phys. B*, **65**, 277–294.
53 Agrawal, G.P. (2007) *Nonlinear Fiber Optics*, 4th edn, Academic Press.
54 Siegman, A.E. (1986) *Lasers*, 1st edn, University Science Books.
55 Desurvire, E., Zyskind, J.L., and Giles, C.R. (1990) Design optimization for efficient erbium-doped fiber amplifiers. *IEEE J. Light. Technol.*, **8**, 1730–1741.
56 Giles, C.R. and Desurvire, E. (1991) Modeling erbium-doped fiber amplifiers. *IEEE J. Light. Technol.*, **9**, 271–283.
57 Coïc, H. (2002) Analytic modelling of high-gain ytterbium-doped fibre amplifiers. *J. Opt. A*, **4**, 120–129.
58 He, F., Price, J.H.V., Vu, K.T., Malinowski, A., Sahu, J.K., and Richardson, D.J. (2006) Optimisation of cascaded Yb fiber amplifier chains using numerical-modelling. *Opt. Express*, **14**, 12846–12858.
59 Mukhodadhyay, P.K., Özgören, K., Bujunoglu, I.L., and Ilday, F.Ö. (2009) All-fiber low-noise high-power femtosecond

Yb-fiber amplifier system seeded by an all-normal dispersion fiber oscillator. *IEEE J. Sel. Top. Quantum Electron.*, **15**, 145–152.

60 Allain, J.Y., Monerie, M., and Poignant, H. (1989) Tunable cw lasing around 0.82, 1.48, 1.88 and 2.35 μm in thulium-doped fluorozirconate fibre. *Electron. Lett.*, **25**, 1660–1662.

61 Walsh, B.M. and Barnes, N.P. (2004) Comparison of Tm:ZBLAN and Tm:silica fiber lasers; spectroscopy and tunable pulsed laser operation around 1.9 μm. *Appl. Phys. B*, **78**, 325–333.

62 Eichhorn, M. (2005) Numerical modeling of Tm-doped double-clad fluoride fiber amplifiers. *IEEE J. Quantum Electron.*, **41**, 1574–1581.

63 Tang, Y. and Xu, J. (2010) High power tunable Tm^{3+}-fiber lasers and its application in pumping Cr^{2+}:ZnSe lasers, in *Frontiers in Guided Wave Optics and Optoelectronics* (ed. B. Pal), InTech, pp. 404–470.

64 Bourdet, G.L. and Lescroart, G. (1999) Theoretical modeling and design of a Tm, Ho:$YLiF_4$ microchip laser. *Appl. Opt.*, **38**, 3275–3281.

65 Percival, R.M., Szebesta, D., Davey, S.T., Swain, N.A., and King, T.A. (1992) High-efficiency cw operation of 890nm pumped holmium fluoride fibre laser. *Electron. Lett.*, **28**, 2064–2066.

66 Kiryanov, A.V., Barmenkov, Y.O., Minkovinch, V.P., and Andres, M.V. (2007) Nonlinear transmission coefficient of ytterbium-holmium fiber at the wavelength 978nm. *Laser Phys.*, **17**, 71–79.

67 Jackson, S.D., Bugge, F., and Erbert, G. (2007) High-power and highly efficient diode-cladding-pumped Ho^{3+}-doped silica fiber lasers. *Opt. Lett.*, **32**, 3349–3351.

68 Brunner, F., Südmeyer, T., Innerhofer, E., Morier-Genoud, F., Paschotta, F., Kisel, V.E., Shcherbitsky, V.G., Kuleshov, N.V., Gao, J., Contag, K., Giesen, A., and Keller, U. (2002) 240-fs pulses with 22-W average power from a mode-locked thin-disk Yb:$KY(WO_4)_2$ laser. *Opt. Lett.*, **27**, 1162–1164.

69 Spühler, G.J., Weingarten, K.J., Grange, R., Krainer, L., Haiml, M., Liverini, V., Golling, M., Schön, S., and Keller, U. (2005) Semiconductor saturable absorber mirror structures with low saturation fluence. *Appl. Phys. B*, **81**, 27–32.

70 Hakulinen, T. and Okhotnikov, O.G. (2007) 8ns fiber laser Q switched by the resonant saturable absorber mirror. *Opt. Lett.*, **32**, 2677–2679.

71 Maas, D.J.H.C., Bellancourt, A.R., Hoffmann, M., Rudin, B., Barbarin, Y., Golling, M., Südmeyer, T., and Keller, U. (2008) Growth parameter optimization for fast quantum dot SESAMs. *Opt. Express*, **16**, 18646–18656.

72 Lagatsky, A.A., Leburn, C.G., Brown, C.T.A., Sibbett, W., Zolotovskaya, S.A., and Rafailov, E.U. (2010) Ultrashort-pulse lasers passively mode locked by quantum-dot-based saturable absorbers. *Prog. Quantum Electronic.*, **34**, 1–45.

73 Chiu, J.C., Lan, Y.F., Chang, C.M., Chen, X.Z., Yeh, C.Y., Lee, C.K., Lin, G.R., Lin, J.J., and Cheng., W.H. (2010) Concentration effect of carbon nanotube based saturable absorber on stabilizing and shortening mode-locked pulses. *Opt. Express*, **18**, 3592–3600.

74 Sun, Z., Hasan, T., Wang, F., Rozhin, A.G., White, I.H., and Ferrari, A.C. (2010) Ultrafast stretched-pulse fiber laser mode-locked by carbon nanotubes. *Nano Res.*, **3**, 404–411.

75 Sun, Z., Hasan, T., Torrisi, F., Popa, D., Privitera, G., Wang, F., Bonaccorso, F., Basko, D.M., and Ferrari, A.C. (2010) Graphene mode-locked ultrafast laser. *ACS Nano*, **4**, 803–810.

76 Sun, Z., Popa, D., Hasan, T., Torrisi, F., Wang, F., Kelleher, E.J.R., Travers, J.C., Nicolosi, V., and Ferrari, A.C. (2010) A stable, wideband tunable, near transform-limited, graphene-mode-locked ultrafast laser. *Nano Res.*, **3**, 653–660.

77 Zhang, H., Tang, D., Zhao, L., Bao, Q., and Loh, K.P. (2010) Vector dissipative solitons in graphene mode locked fiber lasers. *Optics Commun.*, **283**, 3334–3338.

78 Tamura, K., Haus, H.A., and Ippen, E.P. (1992) Self-starting additive pulse mode-locked erbium fibre ring laser. *Electron. Lett.*, **28**, 2226–2228.

79 Hasegawa, A. and Kodama, Y. (1990) Guiding-center soliton in optical fibers. *Opt. Lett.*, **15**, 1443–1444.

80 Blow, K.J. and Doran, N.J. (1991) Average soliton dynamics and the operation of soliton systems with lumped amplifiers. *IEEE Photon. Technol. Lett.*, **3**, 369–379.

81 Kelly, S.M. (1992) Characteristic sideband instability of periodically amplified average soliton. *Electron. Lett.*, **28**, 806–807.

82 Fermann, M.E., Andrejco, M.J., Silberberg, Y., and Weiner, A.M. (1993) Generation of pulses shorter than 200fs from a passively mode-locked Er fiber laser. *Opt. Lett.*, **18**, 48–50.

83 Tamura, K., Ippen, E.P., Haus, H.A., and Nelson, L.E. (1993) 77-fs pulse generation from a stretched-pulse mode-locked all-fiber ring laser. *Opt. Lett.*, **18**, 1080–1082.

84 Smith, N., Knox, F.M., Doran, N.J., Blow, K.J., and Bennion, I. (1996) Enhanced power solitons in optical fiber transmission line. *Electron. Lett.*, **32**, 54–56.

85 Ilday, F.Ö., Buckley, J.R., Clark, W.G., and Wise, F.W. (2004) Self-similar evolution of parabolic pulses in a laser. *Phys. Rev. Lett.*, **92**, 213902.

86 Buckley, J.R., Wise, F.W., Ilday, F.Ö., and Sosnowski, T. (2005) Femtosecond fiber lasers with pulse energies above 10 nj. *Opt. Lett.*, **30**, 1888–1890.

87 Ruehl, A., Prochnow, O., Wandt, D., Kracht, D., Burgoyne, B., Godbout, N., and Lacroix, S. (2006) Dynamics of parabolic pulses in an ultrafast fiber laser. *Opt. Lett.*, **31**, 2734–2736.

88 Anderson, D., Desaix, M., Karlsson, M., Lisak, M., and Quiroga-Teixeiro, M.L. (1993) Wave-breaking-free pulses in nonlinear-optical fibers. *J. Opt. Soc. Am. B*, **10**, 1185–1190.

89 Zhao, L.M., Tang, D.Y., and Wu, J. (2006) Gain-guided soliton in a positive group-dispersion fiber laser. *Opt. Lett.*, **31**, 1788–1790.

90 Chong, A., Buckley, J., Renninger, W.H., and Wise, F. (2006) All normal-dispersion femtosecond fiber laser. *Opt. Express*, **14**, 10095–10100.

91 Chong, A., Renninger, W.H., and Wise, F.W. (2007) All-normal-dispersion femtosecond fiber laser with pulse energy above 20nj. *Opt. Lett.*, **32**, 2408–2410.

92 Bale, B.G. and Wabnitz, S. (2010) Strong spectral filtering for a similariton mode-locked fiber laser. *Opt. Lett.*, **35**, 2466–2468.

93 Oktem, B., Ülgüdür, C., and Ilday, F.Ö. (2010) Soliton-similariton fibre laser. *Nat. Photon.*, **4**, 307–311.

94 Renninger, W.H., Chong, A., and Wise, F.W. (2010) Self-similar pulse evolution in an all-normal-dispersion laser. *Phys. Rev. A*, **82**, 021805(R.

95 Wise, F.W., Chong, A., and Renninger, W.H. (2008) High-energy femtosecond fiber lasers based on pulse propagation at normal dispersion. *Laser Photon. Rev.*, **2**, 58–73.

96 Struwe, M. (1990) *Variational Methods*, 3rd edn, Springer.

97 Anderson, D. (1983) Variational approach to nonlinear pulse propagation in optical fibers. *Phys. Rev. A*, **27**, 3135–3141.

98 Turitsyn, S.K. and Shapiro, E.G. (1998) Variational approach to the design of optical communication systems with dispersion management. *Opt. Fiber Technol.*, **4**, 151–160.

99 Gabitov, I. and Turitsyn, S.K. (1996) Breathing solitons in optical fiber links. *JETP Lett.*, **63**, 863–868.

100 Antonelli, C., Chen, J., and Kärtner, F.X. (2007) Intracavity pulse dynamics and stability for passively mode-locked lasers. *Opt. Express*, **15**, 5919–5924.

101 Bale, B.G. and Kutz, J.N. (2008) Variational method for mode-locked lasers. *J. Opt. Soc. Am. B*, **25**, 1193–1202.

102 Bale, B.G., Boscolo, S., Kutz, J.N., and Turitsyn, S.K. (2010) Intracavity dynamics in high-power mode-locked fiber lasers. *Phys. Rev. A*, **81**, 033828.

103 Malomed, B. (2002) Variational methods in nonlinear fiber optics and related fields, in *Progress in Optics*, vol. **43** (ed. E. Wolf), North-Holland, Amsterdam, ch 2.

104 Vlasov, S.N., Petrishchev, V.A., and Talanov, V.I. (1971) Averaged description

of wave beams in linear media and nonlinear media (the method of moments). *Radiophys. Quantum Electron.*, **14**, 1062–1070.

105 Berkshire, F.H. and Gibbon, J.D. (1983) Collapse in the n-dimensional non-linear Schrodinger equation - a parallel with Sundman results in the n-body problem. *Stud. Appl. Math.*, **69**, 229–262.

106 Marcuse, D. (1992) Rms width of pulses in nonlinear dispersive fibers. *IEEE J. Light. Technol.*, **10**, 17–21.

107 Bélanger, P.A. and Bélanger, N. (1995) Rms characteristics of pulses in nonlinear dispersive lossy fibers. *Opt. Commun.*, **117**, 56–60.

108 Shapiro, E. and Turitsyn, S.K. (1997) Theory of guiding-center breathing soliton propagation in optical communication systems with strong dispersion management. *Opt. Lett.*, **22**, 1544–1546.

109 Turitsyn, S.K. and Mezentsev, V.K. (1998) Dynamics of self-similar dispersion-managed soliton presented in the basis of chirped Gauss-Hermite functions. *JETP Lett.*, **67**, 640–643.

110 Turitsyn, S.K., Schaefer, T., and Mezentsev, V.K. (1998) Self-similar core and oscillatory tails of a path-averaged chirped dispersion-managed optical pulse. *Opt. Lett.*, **23** (17), 1351–1353.

111 Turitsyn, S.K. (1998) Breathing self-similar dynamics and oscillatory tails of the chirped dispersion-managed soliton. *Phys. Rev. E*, **58**, R1256–R1259.

112 Turitsyn, S.K., Aceves, A.B., Jones, C.K.R.T., Zharnitsky, V., and Mezentsev, V.K. (1999) Hamiltonian averaging in soliton-bearing systems with periodically varying dispersion. *Phys. Rev. E*, **59**, R3843–R3846.

113 Usechak, N.G. and Agrawal, G.P. (2005) Semi-analytic technique for analyzing mode-locked lasers. *Opt. Express*, **13**, 2075–2081.

114 Usechak, N.G. and Agrawal, G.P. (2005) Rate-equation approach for frequency modulation mode locking using the moment method. *J. Opt. Soc. Am. B*, **22**, 2570–2580.

115 Turitsyn, S.K., Schaefer, T., and Mezentsev, V.K. (1998) Generalized momentum method to describe high-frequency solitary wave propagation in systems with varying dispersion. *Phys. Rev. E*, **58**, R5264–R5268

116 Turitsyn, S.K. and Shapiro, E.G. (1999) Dispersion-managed soliton in the fiber links with in-line filtering presented in the basis of the chirped Gauss-Hermite. *J. Opt. Soc. Am. B*, **16**, 1321–1331.

117 Shtyrina, O., Fedoruk, M., Turitsyn, S., Herda, R., and Okhotnikov, O. (2009) Evolution and stability of pulse regimes in sesam-mode-locked femtosecond fiber lasers. *J. Opt. Soc. Am. B*, **26** (2), 346–352.

118 Herda, R. and Okhotnikov, O.G. (2004) Dispersion compensation-free fiber laser mode-locked and stabilized by high-contrast saturable absorber mirror. *IEEE J. Quantum Electron.*, **40**, 893–899.

119 Herda, R. and Okhotnikov, O.G. (2005) Effect of amplified spontaneous emission and absorber mirror recovery time on the dynamics of mode-locked fiber lasers. *Appl. Phys. Lett.*, **86**, 011113.

120 Kärtner, F.X., Au, J.A.D., and Keller, U. (1998) Mode-locking with slow and fast saturable absorbers - what's the difference. *IEEE Sel. Top. Quantum Electron.*, **4**, 159–168.

121 Paschotta, R. and Keller, U. (2001) Passive mode locking with slow saturable absorbers. *Appl. Phys. B*, **73**, 653–662.

122 Smith, F.W., Calawa, A.R., Chen, C.L., Manfra, M.J., and Mahoney, L.J. (1988) New MBE buffer used to eliminated backgating in GaAs MESFET's. *IEEE Electron Device Lett.*, **9**, 77–80.

123 Suomalainen, S., Guina, M., Hakulinen, T., Koskinen, R., Paajaste, J., Karjalainen, M., Saarinen, M., Marcinkevicius, S., and Okhotnikov, O.G. (2008) Semiconductor saturable absorbers with recovery time controlled by lattice mismatch and band-gap engineering. *Mater. Sci. Eng. B*, **147**, 156–160.

124 Silverberg, Y., Smith, P.W., Miller, D.A.B., Tell, B., Gossard, A.C., and Wiegmann, W. (1985) Fast nonlinear response from proton-bombarded multiple quantum well structures. *Appl. Phys. Lett.*, **46**, 701–703.

Q5

125 Delpon, E.L., Oudar, J.L., Bouché, N., Raj, R., Shen, A., Stelmakh, N., and Lourtioz, J.M. (1998) Ultrafast excitonic saturable absorption in ion-implanted InGaAs/InAlAs multiple quantum wells. *Appl. Phys. Lett.*, **72**, 759–762.

Q6 126 Okhotnikov, O.G., Grudinin, A., and Pessa, M. (2004) Nonlinear transmission coefficient of ytterbium-holmium fiber at the wavelength 978nm. *New J. Phys.*, **6** (177), 1–22.

127 Gumenyuk, R., Vartiainen, I., Tuovinen, H., Kivistö, S., Chamorovskiy, Y., and Okhotnikov, O.G. (2011) Dispersion compensation technologies for femtosecond fiber system. *Appl. Opt.*, **50**, 797–801.

128 Gumenyuk, R., Vartiainen, I., Tuovinen, H., and Okhotnikov, O.G. (2011) Dissipative dispersion-managed soliton 2 μm thulium/holmium fiber laser. *Opt. Lett.*, **36**, 609–611.

129 Knight, J.C., Broeng, J., Birks, T.A., and Russell, P.S.J. (1998) Photonic band gap guidance in optical fibers. *Science*, **282**, 1476–1478.

130 Lim, H., Ilday, F.Ö., and Wise, F.W. (2002) Femtosecond ytterbium fiber laser with photonic crystal fiber for dispersion control. *Opt. Express*, **25**, 1497–1502.

131 Welch, M.G., Cook, K., Correa, R.A., Géröme, F., Wadsworth, W.J., Gorbach, A.V., Skryabin, D.V., and Knight, J.C. (2009) Solitons in hollow core photonic crystal fiber: engineering nonlinearity and compressing pulses. *J. Light. Technol.*, **27**, 1644–1652.

132 Luan, F., George, A.K., Hedley, T.D., Pearce, G.J., Bird, D.M., Knight, J.C., and Russell, P.St.J. (2004) All-solid photonic bandgap fiber. *Opt. Lett.*, **29**, 2369–2371.

133 Isomäki, A. and Okhotnikov, O.G. (2006) All-fiber ytterbium soliton mode-locked laser with dispersion control by solid-core photonic bandgap fiber. *Opt. Express*, **14**, 4368–4373.

134 Furusawa, K., Monro, T.M., Petropoulos, P., and Richardson, D.J. (2001) Modelocked laser based on ytterbium doped holey fibre. *Elecron. Lett.*, **37**, 560–561.

135 Limpert, J., Schreiber, T., Nolte, S., Zellmer, H., Tünnermann, A., Iliew, R., Lederer, F., Broeng, J., Vienne, G., Petersson, A., and Jakobsen, C. (2003) High-power air-clad large-mode-area photonic crystal fiber laser. *Opt. Express*, **11**, 818–823.

136 Limpert, J., Liem, A., Reich, M., Schreiber, T., Nolte, S., Zellmer, H., Tünnermann, A., Broeng, J., Petersson, A., and Jakobsen, C. (2004) Low-nonlinearity single-transverse-mode ytterbium-doped photonic crystal fiber amplifier. *Opt. Express*, **12**, 1313–1319.

137 Moenster, M., Glas, P., Steinmeyer, G., and Iliew, R. (2004) Mode-locked nd-doped microstructured fiber laser. *Opt. Express*, **12**, 4523–4528.

138 Isomäki, A. and Okhotnikov, O.G. (2006) Femtosecond soliton mode-locked laser based on ytterbium-doped photonic bandgap fiber. *Opt. Express*, **14**, 9238–9243.

139 Snitzer, E. (1961) Proposed fiber cavities for optical lasers. *J. Appl. Phys.*, **32**, 36–39.

140 Maiman, T.H. (1960) Stimulated optical radiation in ruby. *Nature*, **187**, 493–494.

141 Koester, C.J. and Snitzer, E. (1964) Amplification in a fiber laser. *J. Appl. Opt.*, **3**, 1182–1186.

Keywords/Abstract

Dear Author,

Keywords and abstracts will not be included in the print version of your chapter but only in the online version.

Please check and/or supply keywords. If you supplied an abstract with the manuscript, please check the typeset version.

If you did not provide an abstract, the section headings will be displayed instead of an abstract text in the online version.

Keywords: advanced components; dispersion control; modeling; mode-locked fiber lasers; saturable absorber; ultrashort optical pulses.

Q9

Author Query

1. Please note that the style employed by the publisher is for variable vectors to be in bold italics, variables in italics, and labels in Roman; d (differential), e (e^x), π (the constant), i ($\sqrt{-1}$), and ln (natural log) are in also in Roman.
2. Equation 5.1. Please note that the text defines U(z,t) but the equation does not seem to contain this term.
3. Equation 5.2. Please note that here τg is given units of ms, but Table 5.1 has units of μs.
4. Text near the citation of Reference [78]. Please check for clarity the sentence "This, and many other mode-locked fiber lasers that followed, used an operating wavelength of 1.55 μm, where an erbium-doped fiber was used as an amplifying medium and standard telecom fibers have anomalous dispersion." ("... and standard telecom fibers with anomalous dispersion"?).
5. Reference [124]. OK to change the original title of the article as shown (the original title was identical to that in Reference [125])?
6. Reference [126]. OK to give the issue number and page range as shown?
7. Caption to Figure 5.5. OK to amend the caption to "...discrete actions from Equations 5.6 and 5.7 (green lines, black diamonds – the black diamonds are overlapped by the red diamonds defined below)"?
8. Caption to Figure 5.14. OK to amend the original definition of WDM as shown (to match the definition given in the first paragraph of Section 5.3.2.1)?
9. Keywords. Please check that appropriate keywords have been added at the beginning of the chapter (up to six entries are permitted).